



**Assessing the viability of K-Mo₂C for reverse water-gas shift
 scale-up: Molecular to laboratory to pilot scale**

Journal:	<i>Energy & Environmental Science</i>
Manuscript ID	EE-ART-05-2020-001457.R2
Article Type:	Paper
Date Submitted by the Author:	25-Jun-2020
Complete List of Authors:	<p>Juneau, Mitchell; University of Rochester, Chemical Engineering Vonglis, Madeline; University of Rochester, Chemical Engineering Hartvigsen, Joseph; Oxeon Energy LLC Frost, Lyman; Oxeon Energy LLC Bayerl, Dylan; University of Pittsburgh, Department of Chemical and Petroleum Engineering Dixit, Mudit; University of Pittsburgh, Department of Chemical and Petroleum Engineering Mpourmpakis, Giannis; University of Pittsburgh, Chemical and Petroleum Engineering Morse, James; Naval Research Laboratory, Chemistry Baldwin, Jeffrey; U.S. Naval Research Laboratory, Materials Chemistry Branch Willauer, Heather; Naval Research Laboratory, Materials Science Porosoff, Marc; University of Rochester, Chemical Engineering</p>

ARTICLE

Assessing the viability of K-Mo₂C for reverse water-gas shift scale-up: Molecular to laboratory to pilot scale

Received 00th January 20xx,
Accepted 00th January 20xx

DOI: 10.1039/x0xx00000x

Mitchell Juneau,^a Madeline Vonglis,^a Joseph Hartvigsen,^b Lyman Frost,^b Dylan Bayerl,^c Mudit Dixit,^c Giannis Mpourmpakis,^c James R. Morse,^d Jeffrey W. Baldwin,^e Heather D. Willauer,^{d*} Marc D. Porosoff^{a*}

Conversion of CO₂ to value-added chemicals and fuels is a potentially valuable route for renewable energy storage and a future CO₂-neutral economy. The first step is CO₂ conversion to CO via the reverse water-gas shift (RWGS) reaction. Effluent CO can then be hydrogenated to chemicals and fuels via Fischer-Tropsch (FT) synthesis over a tandem catalyst or within a second reactor. To implement this process on an industrial scale, low-cost, scalable and highly-selective catalysts are required, prompting investigations into materials that meet these design constraints. Potassium-promoted molybdenum carbide supported on gamma alumina (K-Mo₂C/γ-Al₂O₃) has recently been shown to be a highly active and selective RWGS catalyst, but the viability and performance of K-Mo₂C/γ-Al₂O₃ for scale-up has not yet been determined. In this report, laboratory-scale (~100 mg catalyst) reactor studies are extended to the pilot-scale (~1 kg catalyst), and viability for scale-up is tested further in the laboratory under a range of temperatures (300 – 600 °C) and flow conditions. The pilot-scale experiments illustrate K-Mo₂C/γ-Al₂O₃ is a highly active and selective catalyst (44% CO₂ conversion, 98%+ CO selectivity at GHSV = 1.7 L kg⁻¹ s⁻¹ and T = 450 °C) that exhibits no signs of deactivation for over 10 days on stream. Together, experiments across the molecular, pilot and laboratory scales demonstrate that K-Mo₂C/γ-Al₂O₃ is an economically-viable RWGS catalyst with promising future applications in the US Naval Research Laboratory's seawater-to-fuel process, downstream methanol synthesis and FT.

Introduction

Consumption of fossil fuels has led to increasing atmospheric and oceanic carbon dioxide concentrations, which are negatively impacting the global environment due to their role in climate change and ocean acidification. In efforts to counteract these negative effects, significant research has been undertaken to develop technologies capable of capturing and converting CO₂ into commodity chemicals and fungible fuels.¹⁻⁶ In recent years, research into direct air capture of CO₂ has expanded, a necessary step to reduce the concentration of atmospheric CO₂.⁷ In a future CO₂-based cyclical economy, the captured CO₂ could be directly input into a CO₂ hydrogenation process to produce chemicals and fuels from CO₂ and renewable H₂.

Currently, the field of CO₂ capture and conversion is experiencing rapid growth as CO₂ is both an abundant and inexpensive C₁ feedstock that can be used as a platform chemical for renewable energy storage.⁸ However, implementation of pilot-scale CO₂ conversion processes is limited by the specific economics of the region. For example, Canada and Iceland have both undertaken CO₂ capture and conversion efforts to produce synthetic fuels and methanol, respectively.^{9, 10} Within pilot-scale CO₂ conversion processes, CO₂ hydrogenation is typically conducted thermochemically via modified Fischer-Tropsch (FT) synthesis, with CO₂ substituted for the CO reactant (CO₂-FT).¹¹⁻¹⁵ In CO₂-FT, CO₂ is first converted to CO via endothermic reverse water-gas shift (RWGS, Scheme 1), followed by subsequent hydrogenation of CO to hydrocarbon products via exothermic FT. Therefore, to achieve high yield toward the desired hydrocarbon products (C₆+), the equilibrium-limited RWGS reaction is typically operated at high temperatures (>600 °C) to achieve high CO₂ conversion and prevent CO₂ from entering the downstream FT reactor where it can be converted to undesired CH₄ via the Sabatier reaction.¹⁶

Achieving high selectivity toward desirable CO for downstream FT at more moderate temperatures (~450 °C) with lower energy input is difficult because the methanation and Sabatier side reactions (Schemes 2 and 3) are highly thermodynamically favorable under these lower temperature RWGS conditions.¹⁷

^a Department of Chemical Engineering, University of Rochester, Rochester, NY, 14627, USA; Email: marc.porosoff@rochester.edu

^b OxEon Energy, LLC, North Salt Lake, UT, 84054, USA.

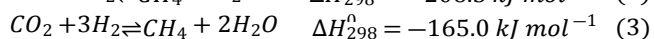
^c Department of Chemical and Petroleum Engineering, University of Pittsburgh, Pittsburgh, PA, 15261, USA.

^d Materials Science and Technology Division, Naval Research Laboratory, Washington DC, 20375, USA.

^e Acoustics Division, Naval Research Laboratory, Washington, DC, 20375, USA.

* Corresponding Author

Electronic Supplementary Information (ESI) available: [ESI includes further details on pilot-scale synthesis and characterization, along with laboratory-scale performance and characterization information and DFT structural configurations]. See DOI: 10.1039/x0xx00000x



One option for achieving high performance during RWGS is to use well-established forward water-gas shift catalysts for the reverse reaction.^{18, 19} As shown in Figure 1 (sample calculations are included in the Supporting Information), the low temperature industrial catalyst (Cu-ZnO/Al₂O₃) is a top performing catalyst at 300 °C with a CO space-time yield (STY) of 80.2 μmol CO gcat⁻¹ s⁻¹ and CO selectivity of 92.6%. However, the high temperature industrial catalyst (FeCrO_x) performs poorly at 450 °C with a CO STY of 21.5 μmol CO gcat⁻¹ s⁻¹ because of a low CO selectivity of 48.6%.

Precious metal-based catalysts are also promising candidates for RWGS.^{20, 21} Recent studies show that for RWGS over Rh supported on silicalite-1 (S-1) at 450 °C and Pt supported on TiO₂ at 400 °C result in high CO selectivities of 71.3% and 100% and CO STYs of 3.0 μmol CO gcat⁻¹ s⁻¹ and 5.0 μmol CO gcat⁻¹ s⁻¹, respectively.^{22, 23} However, Pt-based catalysts exhibit deactivation and decreased selectivity toward CO with increased time-on-stream, limiting their applicability in a scaled-up process.²⁴ Additionally, the high material costs of Rh and Pt result in a high cost of CO when compared to other top-performing transition metal catalysts, as shown in Figure 1. For example, at 400 °C with a 4:1 H₂:CO₂ ratio, Fe and Cu supported on CeO₂ exhibit reasonable CO₂ conversions of 8.1% and 31.3%, both with 100% CO selectivities at atmospheric pressure and a moderately high GHSV (16.7 L kg⁻¹ s⁻¹),²⁵ resulting in a very low cost of CO when compared to the precious metal catalysts.

Other low-cost alternatives to precious metal catalysts are transition metal carbides (TMCs), which exhibit comparable activity and selectivity to their precious metal counterparts for many reactions, including RWGS.²⁶ These observed experimental trends have been corroborated with density functional theory (DFT) calculations, indicating that incorporation of carbon into the transition metal lattice attenuates the electronic properties of the catalyst, and in turn, adsorption of the reactants, intermediates and products.²⁷⁻²⁹ Detailed investigations into TMCs for RWGS have shown that unsupported Mo₂C can outperform commonly used Pt and Pd-based bimetallic catalysts,³⁰⁻³² while supported Mo₂C and WC are also active and selective for producing CO via RWGS.^{33, 34} The higher activity observed over TMCs is a result of CO₂ activation occurring via direct C=O bond scission, without formation of any carbonates or formates, the typical intermediates observed over precious metal-based catalysts.³⁵

To further improve the catalytic properties of TMCs for RWGS, alkali metals are incorporated into the catalyst matrix as low-cost promoters to attenuate the electronic and structural properties of the TMC,^{27, 34, 36} resulting in increased CO₂ binding energy and a decreased energy barrier for CO₂ dissociation.³⁷⁻³⁹ These results are confirmed in reactor studies of potassium promoted Mo₂C and WC supported on γ-Al₂O₃, which both show an increase in CO selectivity and stability during RWGS.^{40, 41} The favorable catalytic properties of alkali-promoted TMCs along with their low-cost and facile synthesis suggest that these

catalysts, and K-Mo₂C in particular, have high potential for scale-up.

When evaluating a catalyst for scale-up, it is important to synthesize the catalyst with a scalable synthesis method, such as wet impregnation, using low-cost materials. Once synthesized, the catalyst must exhibit high stability over thousands of hours on stream and be easily regenerable to maximize catalyst lifetime.^{42, 43} It is also necessary to consider the reactor operating conditions, CO purity and cost of CO. Investigations are performed at varying temperatures and gas hourly space velocities (GHSVs), requiring metrics to better describe the scalability of top-performing laboratory-scale RWGS catalysts. As shown in Figure 1, with specific conditions and detailed performance of additional catalysts found in Table 4 (discussion section), we have demonstrated in the current work that the low-cost and highly active catalyst, K-Mo₂C/γ-Al₂O₃ is overall the top performing catalyst for RWGS, when accounting for CO purity, CO STY and the cost of the catalyst per kg of CO produced. To better understand the high performance of K-Mo₂C/γ-Al₂O₃ and applicability in an industrial process, we have performed a detailed study of the catalyst performance across different scales, from molecular to laboratory to pilot.

In this paper, laboratory and pilot-scale reactor experiments are combined with DFT calculations and catalyst characterization using X-ray diffraction (XRD), X-ray photoelectron spectroscopy (XPS) and pulse chemisorption to show that K-Mo₂C/γ-Al₂O₃ is a highly active, selective and stable RWGS catalyst. The pilot-scale catalyst, P-K-Mo₂C/γ-Al₂O₃, is synthesized on an industrial γ-Al₂O₃ trilobe support, and high performance is first demonstrated in the laboratory with CO selectivity greater than 99% over 100 h+ on stream at 450 °C. At very high temperature (600 °C), CH₄ becomes the primary product, likely because of coking and oxidation of the active phase.

Extending the results of P-K-Mo₂C/γ-Al₂O₃ to the kilogram scale in a pilot reactor at OxEon Energy (Figure 2) at 450 °C and a gas hourly space velocity of 1.7 L kg⁻¹ s⁻¹, results in CO selectivities >98% with no signs of deactivation after 10 days on stream. The combined laboratory and pilot-scale experiments clearly demonstrate K-Mo₂C/γ-Al₂O₃ is a low-cost, high performance RWGS catalyst, suitable for scale-up and integration into high throughput processes to convert CO₂ into value-added chemicals and fuels.

Experimental

Laboratory-scale (L-K-Mo₂C/γ-Al₂O₃) catalyst preparation: The laboratory-scale K-Mo₂C was synthesized on γ-Al₂O₃ (Alfa Aesar, 99.97% pure, 3 Micron APS Powder) via incipient wetness impregnation of potassium nitrate (Alfa Aesar, 99.995% pure) and ammonium molybdate (para) tetrahydrate (Alfa Aesar, 99% pure) with a target of 2 wt% K and 20 wt% Mo loading for a target molar ratio of 1/4/15 K/Mo/γ-Al₂O₃. The catalysts were dried at 35 °C, calcined at 350 °C with 5 °C min⁻¹ ramp rate, and then carburized at 600 °C in a 21% CH₄/H₂ mixture for 5 h. After carburization, the catalyst was passivated in a 1% O₂/N₂ gas mixture.

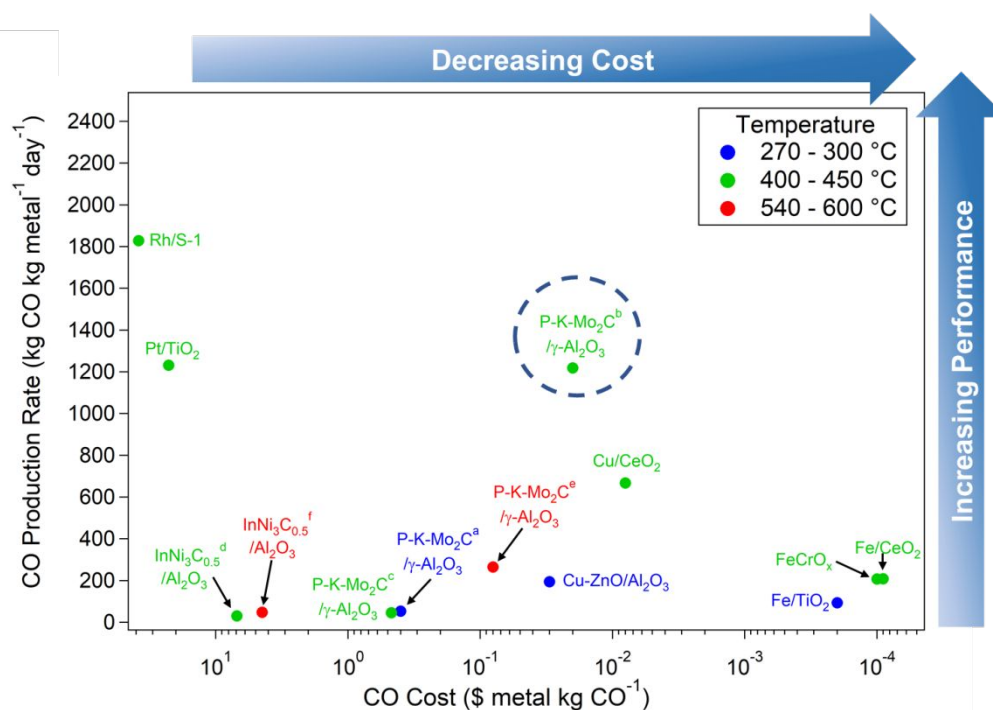


Figure 1. Metrics for comparing state-of-the-art RWGS catalysts. CO production rate ($\text{kg CO kg metal}^{-1} \text{ day}^{-1}$) is plotted versus CO cost ($\text{\$ metal kg CO}^{-1}$) for selected catalysts. Sample calculations for CO production rate and CO cost are included in the Supporting Information and specific reaction conditions with detailed performance for each catalyst are found in Table 4 (discussion section). P-K-Mo₂C/ γ -Al₂O₃ reaction conditions are as follows: a) 300 °C, 2.1 MPa, 36.7 L kg⁻¹ s⁻¹; b) 450 °C, 2.1 MPa, 36.7 L kg⁻¹ s⁻¹; c) 450 °C, 0.1 MPa, 1.8 L kg⁻¹ s⁻¹; e) 600 °C, 2.1 MPa, 3.7 L kg⁻¹ s⁻¹. InNi₃C_{0.5}/Al₂O₃ reaction conditions are as follows: d) 420 °C, 1 MPa, 1.7 L kg⁻¹ s⁻¹; f) 540 °C, 1 MPa, 1.7 L kg⁻¹ s⁻¹.

Pilot-scale (P-K-Mo₂C/ γ -Al₂O₃) catalyst preparation: The pilot-scale K-Mo₂C was synthesized on trilobe γ -Al₂O₃ via 3-step incipient wetness impregnation with target molar ratios of 1/4/15 K/Mo/ γ -Al₂O₃, using the same potassium and molybdenum precursors as the laboratory-scale catalyst. After drying, the catalyst was calcined for 6 h at 350 °C, followed by carburization at 660 °C for 4 h in a 21% CH₄ in H₂ gas mixture. The higher carburization temperature was necessary because of a lack of carbide phase observed after 600 °C carburization. The catalyst was then passivated in 5% O₂ in N₂. To synthesize P-K-Mo₂C under laboratory-scale conditions (LC-P-Mo₂C), after carburization the catalyst was oxidized at 350 °C under static air conditions in a muffle furnace and then recarburized and passivated according to the above laboratory-scale (L-K-Mo₂C/ γ -Al₂O₃) catalyst preparation. Additional details of the pilot-scale catalyst synthesis can be found in Figures S1-S5 and Tables S1-S2 of the Supporting Information.

X-ray diffraction (XRD): XRD patterns of the catalysts were recorded on a Malvern Panalytical multi-purpose diffractometer using CuK α radiation operated at 40 kV and 30 mA over the range of $2\theta = 5\text{--}70^\circ$ with a 0.03° step size and 0.5 s per step at room temperature. PDFs used for peak assignment: MoO₂ [PDF: 00-032-0671], Mo₂C [PDF: 00-035-0787], MoC [PDF: 00-045-1015] and γ -Al₂O₃ [PDF: 00-050-0741].

Laboratory-scale reactor studies: To measure the catalytic performance for RWGS, laboratory-scale flow reactor studies were performed with 50 mg to 1 g of catalyst, depending on the desired GHSV, packed in a 1/2" diameter, 12" long, stainless steel reactor and reduced under 40 sccm H₂ for 2 h at 300 °C and 0.34

MPa. After reduction, the reactor was isolated and the bypass pressurized to 2.1 MPa with specific gas flow rates and catalyst loadings to reach the desired GHSV.

Unless otherwise noted, reactions were run for 12 h at 300 °C, 450 °C and 600 °C at 2.1 MPa with a 3:1 H₂:CO₂ ratio. For laboratory-scale RWGS reaction experiments, reactant flow rates of 30 sccm of H₂, 10 sccm of CO₂ and 5 sccm of Ar as an internal standard were typically used, but for time-on-stream studies, flow rates were increased to 75 sccm of H₂, 25 sccm of CO₂ and 10 sccm of Ar to maintain the H₂:CO₂ ratio at 3:1. Concentrations of reactants and products were analyzed by an in-line Agilent Technologies 7890B gas chromatograph equipped with a flame ionization detector (FID) and a thermal conductivity detector (TCD). The concentration of each gas-phase species was calibrated by correlating the peak area of the pure compound to its concentration in a calibration gas standard. The industrial FeCrO_x used as comparison for laboratory-scale reactor studies was an Alfa Aesar iron-chrome based high temperature water-gas shift catalyst, HiFUEL® W210. The industrial Cu-ZnO/Al₂O₃ catalyst was an Alfa Aesar copper-based low temperature water-gas shift catalyst, HiFUEL® W220.

Pilot-scale reactor studies: All pilot-scale experiments were conducted by OxEon Energy LLC. The OxEon Energy pilot gas-to-liquids (GTL) system included a natural gas reformer, syngas compression and storage, and a Fischer-Tropsch reactor with cooling loop and recycle. For testing the P-K-Mo₂C/ γ -Al₂O₃ catalyst, the syngas compressor was fed by a bulk CO₂ tank and dual hydrogen tank clusters (18 x 300 SCF high pressure cylinders), which compressed a 3:1 mixture of H₂:CO₂ to ~1.4



Figure 2. Pilot-scale reactor with (left) and without (right) insulation, where band heaters are visible and wrapped around the reactor. The full piping and instrumentation diagram is available in Figure S6 of the Supporting Information.

MPa, where it was then stored in a 240 gal tank. The 240 gal tank fed a second compressor, which compressed the feed to ~5.2 MPa, which was then stored in two 500 gal holding tanks. Next, the high pressure feed was regulated down to the inlet reactor pressure of 2.1 MPa and metered through a control valve with a mass flow meter.

For reverse water-gas shift, the reactor was customized with a 4" diameter sch. 10 stainless steel pipe with an aluminum fin insert to improve heat transfer from the band heaters to the P-K-Mo₂C/γ-Al₂O₃ catalyst. The temperature of the reactor was monitored with a thermocouple near the exit of the reactor, while the inlet side of the reactor was charged with aluminum shot to enhance preheating of the reactor feed to 250 °C. Gas exiting the reactor then entered hot and cold traps, the recycle compressor and the back pressure regulator. This reaction produced a stoichiometric amount of water that was captured by a cold trap at 6 °C. The effluent products and residual reactants from the RWGS reactor were sampled by a microchannel gas chromatograph and logged into Labview. For calculating conversion and selectivity, approximately 8% of the reactor feed was comprised by N₂ as an internal standard.

DFT calculations of CO₂ and CO adsorption on Mo₂C: Density functional theory (DFT) calculations were performed within the projector-augmented wave (PAW) method as implemented in the VASP plane-wave DFT software package.⁴⁴ The approach was similar to previous work,^{45, 46} which utilized the Perdew-Burke-Ernzerhof (PBE) formulation⁴⁷ of the generalized-gradient approximation (GGA) to the exchange-correlation functional, a 415 eV plane-wave cutoff, gamma-centered 5 × 5 × 1 k-point grid, 10⁻⁶ eV electronic energy convergence criterion, 0.01 eV Å⁻¹ force convergence criterion, and 1st-order Methfessel-Paxton occupation smearing⁴⁸ with 0.2 eV broadening. The supercell consisted of adsorbates plus a slab of 2 × 2 × 1 unit cells of orthorhombic β-Mo₂C (48 slab atoms) representing 1.27 nm² of the (001) facet. Slabs were

constructed with opposing Mo-terminated and C-terminated facets separated by 1.0 nm of vacuum.

Adsorption of CO₂ and CO on the clean, Mo-terminated Mo₂C (001) facet was considered, as well as in the presence of co-adsorbed oxygen (an oxygen atom bound to each of four available hollow sites). CO₂ and CO coverages ranged from 0.25 ML (two molecules) to 1 ML (eight molecules). The uppermost Mo and C layers and the adsorbates were allowed to relax, while slab atoms in the lowermost Mo and C layers were fixed in their bulk positions. Supercell dimensions were also fixed during relaxation (1.050 nm × 1.215 nm × 1.455 nm), with in-plane lattice constants of 0.5250 nm and 0.6073 nm obtained from relaxation of the bulk unit cell (in good agreement with experimental values⁴⁹ of 0.5195 nm and 0.6022 nm, respectively).

The binding energy per molecule on the surface was calculated using the following equation: $BE_{ads} = (E[N_{ads}@Mo_2C(001)] - E[Mo_2C(001)] - N_{ads}E_{ads})/N_{ads}$, where $E[N_{ads}@Mo_2C(001)]$ was the energy of N_{ads} CO or CO₂ molecules adsorbed on the clean (or oxidized) Mo₂C (001) surface, $E[Mo_2C(001)]$ was the energy of the clean (or oxidized) Mo₂C surface, and E_{ads} was the energy of the CO or CO₂ molecule in the gas phase.

X-ray photoelectron spectroscopy (XPS): XPS spectra were gathered over the fresh and spent catalysts using a Kratos Axis Ultra DLD XPS spectrometer equipped with a mono-ALKα X-ray source (1468.6 eV). The XPS spectra were collected using the slot aperture analyzer settings (~300 × 700 μm substrate area). Three sweeps were recorded for the survey and regional scans to increase signal-to-noise ratio. The electron collection angle, θ, in all XPS measurements was zero. Settings for data collection were: Pass Energy = 20 eV, dwell time = 200 ms, energy step size = 0.1 eV. Charge compensation was necessary. Calibration of the instrument was confirmed with C1s peak of carbon tape at 284.6 eV. The XPS signal areas were measured using Casa XPS software.

N₂ physisorption according to BET method: N₂ physisorption measurements according to BET method were performed using a Micromeritics ASAP 2020 BET Analyzer at -196 °C to determine catalyst surface area. All of the catalysts were degassed at 350 °C for 2 h under vacuum before analysis.

Pulse chemisorption: Pulse chemisorption experiments were performed using a Micromeritics AutoChem II 2920, where the probe gas (CO₂ or CO) was pulsed ten times over 50 mg of catalyst at 35 °C to determine the adsorption behavior of the probe molecule. Prior to each measurement, the catalyst was reduced in H₂ for 2 h at 300 °C. Immediately following pulse chemisorption, temperature programmed desorption (TPD) experiments were performed, using the same sample and experimental setup while ramping from 25 °C to 800 °C at a rate of 5 °C/min under inert He carrier gas flowing at 10 sccm. The blank TPD experiments were performed using the same procedure, but without the pulse chemisorption step.

X-ray absorption fine structure (XAFS): X-ray absorption fine structure (XAFS) measurements were used to assess the stability of the P-K-Mo₂C catalyst *in situ*. XAFS measurements of the Mo K-edge were performed on the 8-ID (ISS) beamline at the National Synchrotron Light Source (NSLS-II), Brookhaven National Laboratory. Catalysts were diluted with boron nitride, pressed into a pellet, and grinded and sieved between 200–350 μm. The prepared catalyst was then loaded into a custom designed cell with glassy carbon tube with heater and gas connections.⁵⁰ The catalysts were reduced *in situ* under hydrogen flow (40 sccm) at 300 °C for 2 h and XAFS data of the Mo K-edge were collected under hydrogen after cooling to room temperature. CO₂ hydrogenation was performed *in situ* under CO₂ and hydrogen flow at 10 sccm and 30 sccm, respectively at 450 °C and 600 °C for 4 h at each temperature. For each temperature, XAFS data of the Mo K-edge were again collected under reaction gases after cooling to room temperature. The incident and transmitted X-ray signals were collected with ionization chambers while the fluorescence signal was collected using a passivated implanted planar silicon (PIPS) detector. The XAFS spectra from the samples were calibrated to a Mo₂C standard (Alfa Aesar) collected in transmission mode. The X-ray signal was analyzed using the Demeter 0.2.96 data analysis package (Athena, Aretmis, Atoms, and FEFF6).^{51, 52}

Results

X-ray Diffraction

In addition to the pilot-scale K-Mo₂C catalyst supported on γ-Al₂O₃ trilobes (P-K-Mo₂C/γ-Al₂O₃), laboratory-scale K-Mo₂C supported on γ-Al₂O₃ powder (L-K-Mo₂C/γ-Al₂O₃) has been synthesized as a reference for comparison with previous work, to assess any discrepancies between the catalysts synthesized on each scale.⁴¹ As a first step to validate synthesis of P-K-Mo₂C/γ-Al₂O₃, the pilot and laboratory-scale catalysts are characterized using X-ray diffraction (XRD).

For P-K-Mo₂C/γ-Al₂O₃, the XRD patterns in Figure 3 indicate the catalyst is comprised of MoO₂ [PDF: 00-032-0671] and β-Mo₂C [PDF: 00-035-0787], with large discrete peaks observed at 26.2°, 37.0°, 53.4°, and 60.5° for MoO₂ and 39.3° and 73.4° for β-Mo₂C, suggesting incomplete carburization.⁴¹ Additionally, MoC peaks [PDF: 00-045-1015] are identified at 2θ = 35.5°, 49.0° and 63.8°. Reflections due to the trilobe γ-Al₂O₃ support [PDF: 00-050-0741] are observed at 2θ = 37.5°, 45.5° and 67.0°.

For the laboratory as-synthesized catalyst (L-K-Mo₂C/γ-Al₂O₃), no MoO₂ or MoC phases are observed and the reflections corresponding to β-Mo₂C (2θ = 34.7°, 39.5° and 61.6°) are observed at relative intensities greatly exceeding that of P-K-Mo₂C/γ-Al₂O₃, suggesting more complete carburization of L-K-Mo₂C/γ-Al₂O₃. This is most likely due to longer carburization of the laboratory-scale catalyst (5 h for L-K-Mo₂C versus 4 h for P-K-Mo₂C) and improved mass transfer over the γ-Al₂O₃ powder versus the γ-Al₂O₃ trilobes, even though the P-

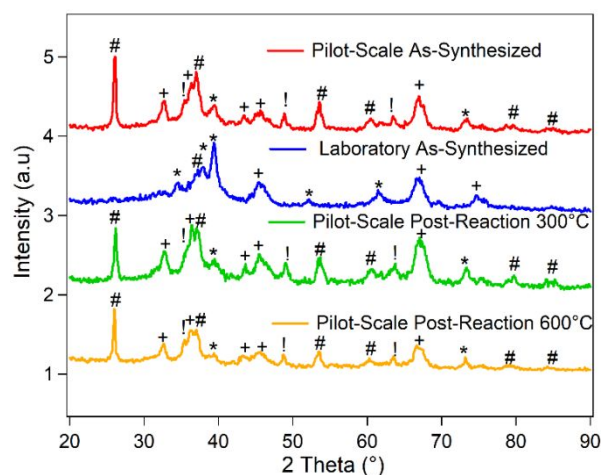


Figure 3. X-ray diffraction patterns of K-Mo₂C/γ-Al₂O₃. Symbols correspond to: γ-Al₂O₃ (+), MoO₂ (#), β-Mo₂C (*), and MoC (!).

K-Mo₂C/γ-Al₂O₃ is carburized at a higher temperature of 660 °C, versus 600 °C for L-K-Mo₂C/γ-Al₂O₃.

Reactor Studies

To first evaluate the performance of the pilot-scale catalyst, P-K-Mo₂C/γ-Al₂O₃, measurements are conducted at the laboratory-scale at several temperatures and under a variety of flow conditions to estimate the ideal experimental regime for pilot-scale studies. As seen in Figure 4, at 300 °C, the CO yield is substantially below the equilibrium value, and decreases slightly as the GHSV is increased. This suggests the reaction is kinetically limited at the highest GHSV of 36.7 L kg⁻¹ s⁻¹ at 300 °C. When the temperature is increased to 450 °C, the CO yield approaches equilibrium at 1.8 – 3.7 L kg⁻¹ s⁻¹, but at the highest GHSV of 36.7 L kg⁻¹ s⁻¹, the reaction is kinetically limited. However, at 600 °C, the CO yield approaches equilibrium at the higher GHSVs, 3.7 and 36.7 L kg⁻¹ s⁻¹, likely because of longer space-time at the low GHSV of 1.8 L kg⁻¹ s⁻¹ resulting in increased CO₂ methanation. A summary of the laboratory-scale RWGS experiments over P-K-Mo₂C/γ-Al₂O₃ at each temperature and GHSV can be found in Table 1.

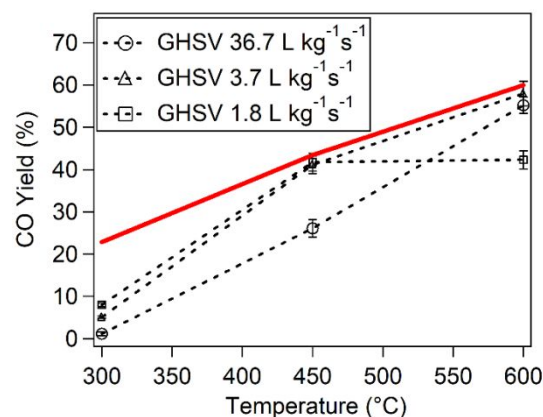


Figure 4. Performance of P-K-Mo₂C/γ-Al₂O₃ during RWGS at 300 °C, 450 °C and 600 °C at the laboratory-scale as a function of GHSV. The thermodynamic equilibrium CO yield is plotted as a red solid line. All reactor studies are using a 3:1 H₂:CO₂ reactant ratio at 2.1 MPa. All data points are the average of 18 steady-state data points, taken between 7 – 12 h on stream.

Table 1. Summary of P-K-Mo₂C/γ-Al₂O₃ laboratory-scale reactor performance for RWGS at 2.1 MPa and 3:1 H₂:CO₂ ratio as a function of temperature and GHSV. All data points are the average of 18 steady-state data points, taken between 7 - 12 h on stream. In all cases, no oxygenates are detected.

T (°C)	GHSV (L s ⁻¹ kg ⁻¹)	Conversion (%)	Carbon-based Selectivity (%)					Carbon Balance (%)	CO Yield (%)
			CO	CH ₄	C ₂ H ₆	C ₂ H ₄	C ₃ +		
300	1.1	8.9	99.2	0.6	0.1	0	0	99.4	8.8
300	1.8	8.4	94.9	2.7	1.0	0.1	1.2	99.1	8.0
300	3.7	5.2	98.6	1.1	0.3	0	0	99.2	5.1
300	18.3	2.1	95.7	4.3	0.0	0	0	98.8	2.0
300	36.7	1.2	99.2	0.8	0.0	0	0	99.6	1.2
450	1.1	43.3	95.7	3.5	0.6	0.03	0.15	97.8	41.5
450	1.8	42.1	99.1	0.8	0.1	0	0	100.4	41.7
450	3.7	41.5	99.3	0.5	0.1	0.02	0.14	99.0	41.2
450	18.3	33.0	99.9	0.1	0.0	0.01	0	98.3	33.0
450	36.7	26.2	99.9	0.0	0.0	0.02	0	99.5	26.1
600	1.1	58.5	65.8	31.2	2.7	0	0.3	96.4	38.5
600	1.8	57.6	73.6	23.3	2.7	0	0.5	97.2	42.3
600	3.7	59.0	98.3	1.6	0.1	0	0	98.1	57.9
600	18.3	59.2	98.5	1.4	0.1	0.03	0.03	96.9	58.3
600	36.7	56.3	98.0	1.8	0.1	0.02	0.02	97.9	55.2

To further elaborate on the data contained in Table 1 at 300 °C and 450 °C, there is a decrease in conversion at increasing GHSV, while CO selectivity remains relatively constant. At 600 °C, there is a slightly different trend, where the conversion is relatively constant, but CO selectivity increases with GHSV because of shorter spacetimes in the reactor, suggesting a CO₂ → CO → CH₄ mechanism, consistent with work completed by Shi et al.^{28, 53} All data in Table 1 are from steady-state data points averaged between 7-12 h on stream, and it is expected with additional time-on-stream, that the CO selectivities of all 600 °C trials would decrease to ~65%, as shown in the stability measurements in Figure 5. Additional figures showing the detailed reactor performance of P-K-Mo₂C/γ-Al₂O₃ at each temperature as a function of GHSV can be found in the Supporting Information (Figures S7 – S9).

From detailed analysis of our laboratory-scale reactor studies in Figure 4, 450 °C is determined to be the optimal temperature for pilot-scale measurements. At the lower temperature of 300 °C, P-K-Mo₂C does not display exceptional performance when compared to other non-precious metal catalysts or the industrial water-gas shift catalyst, Cu-ZnO/Al₂O₃, as shown in Figure 1 and Table 4. At 600 °C, the P-K-Mo₂C catalyst transitions from a highly selective RWGS catalyst to a methanation catalyst after only ~14 h on stream, as shown in Figure 5. Therefore, 450 °C is the most appropriate temperature for pilot-scale studies, because at this temperature, P-K-Mo₂C demonstrates high CO₂ conversion, CO selectivity and stability.

As shown in Figure 6 for the scaled-up reactor studies of P-K-Mo₂C/γ-Al₂O₃, the catalyst displays consistently high CO₂

conversion and CO selectivity at 450 °C across a range of GHSVs. The piping and instrumentation diagram for the pilot-scale reactor is included in Figure S6 of the Supporting Information.

The CO yield for the data point at the GHSV of ~0.5 L kg⁻¹ s⁻¹ in Figure 6 appears to exceed the maximum thermodynamic equilibrium, but this is likely an artifact of slight variations in the inlet reactant mixture at flow rates greater than 60 standard liters per minute (SLPM) during the pilot-scale studies. The actual values of CO₂ conversion must be slightly lower than the values reported in Figure 6, which would result in CO yields just below the thermodynamic equilibrium. Similar to the laboratory-scale experiments, the performance of P-K-Mo₂C/γ-Al₂O₃ at 450 °C does not appear to be a strong function of GHSV, which is likely due to thermodynamic limitations of the reaction under the tested conditions. Higher flow conditions could not be tested at the pilot-scale because the experimental apparatus (details in the experimental section) prevented the H₂ flow rate from exceeding ~150 SLPM.

The observed equilibrium limitations of the pilot-scale reactor experiments at 450 °C, shown in Figure 6, require additional experiments at higher GHSVs to both determine the catalytic performance in the kinetically limited regime and accurately assess the stability for future scale-up. As shown in the stability measurements in Figure 5, laboratory-scale, time-on-stream reactor studies of P-K-Mo₂C/γ-Al₂O₃ at 450 °C and a GHSV of 36.7 L kg⁻¹ s⁻¹, exhibit no signs of deactivation for 120 h+ on stream, with a CO yield and STY equal to 26.6% and 99.1 μmol CO g⁻¹ s⁻¹, respectively. This suggests that during scale-up, GHSVs can be used that are ~20x faster than those in the pilot-scale study to maximize the CO STY at 450 °C.

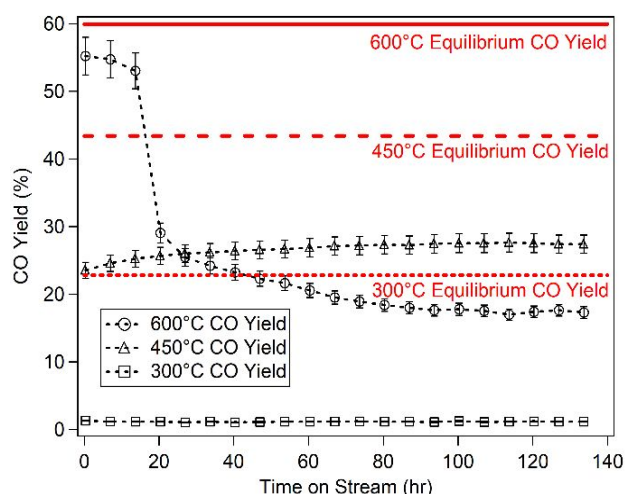


Figure 5. Laboratory-scale performance of P-K-Mo₂C/γ-Al₂O₃ during RWGS for 120 h on stream. CO yield versus time-on-stream is plotted for experimental data (markers) and the equilibrium maximum CO yields (red lines) at each temperature. Experiments are all at a GHSV of 36.7 L kg⁻¹ s⁻¹ with a 3:1 H₂:CO₂ reactant ratio at the temperatures listed (300 °C, 450 °C, 600 °C) and 2.1 MPa.

For time-on-stream experiments at 300 °C, the CO yield is also stable at 1.2%, but there is a significant decrease (~71%) observed in the CO yield of the catalyst tested at 600 °C after ~14 h on stream. The conversion over the catalyst tested at 600 °C remains relatively constant, but the decrease in CO yield is due to a substantial decrease in CO selectivity with a corresponding increase in CH₄ selectivity. After regenerating the catalyst with H₂ for 2 h at 300 °C, the CO selectivity recovers slightly from 28.8% to 41.0%, but does not reach the original value of 98.1%.

Although the single-pass CO yield is thermodynamically limited to 43.4% at 450 °C with a 3:1 H₂:CO₂ ratio, the maximum CO yield can be increased by recycling the single-pass product stream, as shown in Figure 7. With each recycle trial, the fresh feed flow rate is kept constant at 60 SLPM and a fraction of the reactor effluent is chilled to 6 °C to remove water, preheated, and then mixed with the fresh feed to yield GHSVs over the catalyst from 1.7 L kg⁻¹ s⁻¹ to 5.1 L kg⁻¹ s⁻¹. The recycle ratio

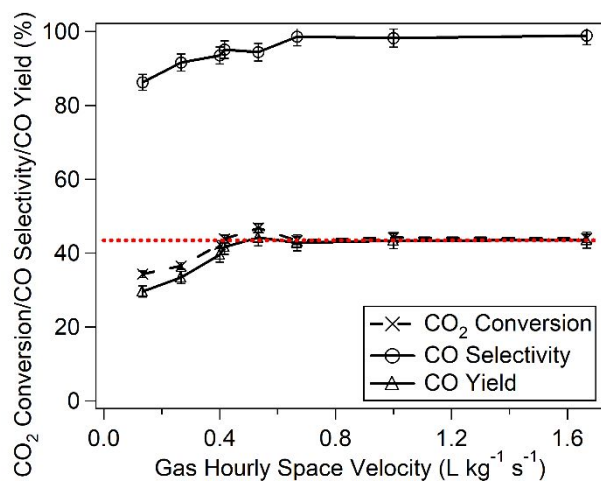


Figure 6. Pilot-scale reactor performance of P-K-Mo₂C/γ-Al₂O₃ during RWGS with CO₂ conversion, CO selectivity and CO yield plotted versus GHSV. The thermodynamically limited equilibrium CO yield of RWGS is included as a dotted red line. All reactor studies are for a 3:1 H₂:CO₂ reactant ratio at 450 °C and 2.1 MPa.

plotted in Figure 7 is the ratio between the molar flow rate of the recycled reactor effluent and the fresh feed entering the reactor. As shown in the figure, the CO₂ conversion increases steadily as a function of recycle ratio, as expected.

It is also observed that the CO selectivity decreases with increasing recycle ratio, suggesting that the longer average residence times of CO₂ and CO within the reactor result in higher conversion, but lower CO selectivity. At the highest recycle ratio of 2, the reactor effluent is ~18% CO and only 5.6% CO₂, indicating the outlet CO:CO₂ ratio is ~3, while during single pass conversion the outlet CO:CO₂ ratio is ~0.8. Therefore, the higher concentration of CO combined with greater residence time during recycle, results in a larger fraction of CO hydrogenated to undesired CH₄. However, CO selectivity remains above 92% in all cases, demonstrating recycling is an effective tool to increase the CO yield at lower temperatures. It is also important to note that all pilot-scale studies were conducted sequentially without any re-activation steps. Total time-on-stream was approximately 10 days and the catalyst exhibited no signs of deactivation.

Density Functional Theory Calculations

In an effort to better explain the decreasing CO selectivity at high recycle ratios, DFT calculations are shown in Figures 8 and 9 to quantify the strength of CO₂ and CO adsorption over clean Mo₂C and Mo₂C modified with oxygen, which models the active oxycarbide phase of the RWGS reaction.³⁰ As shown in Figure 8, CO₂ and CO both adsorb favorably to Mo₂C and oxygen-modified Mo₂C.⁵⁴ Closer inspection of the figure reveals that at all CO₂ and CO coverages between 0.25 and 1 ML, CO adsorbs more strongly than CO₂ to the Mo₂C-based surface. This is an important result that corroborates the findings of the pilot-scale recycle study where a decrease in CO selectivity is observed at high recycle ratios. A likely cause of the decreasing CO selectivity is that during single pass conversion, CO₂ is the primary carbon-based species in the reactor and has active sites available for reaction, resulting in a CO selectivity of 98.2%. As

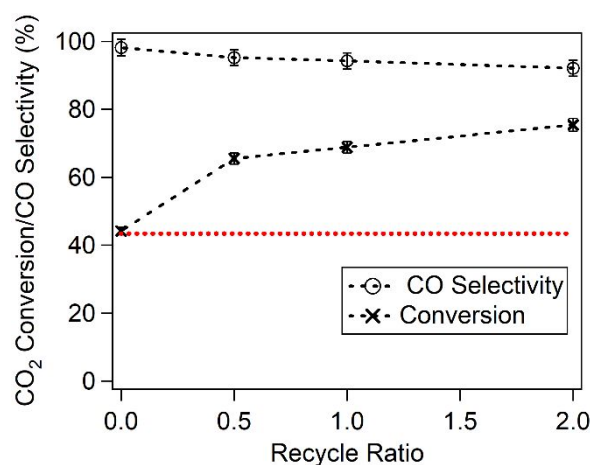


Figure 7. Pilot-scale reactor performance of P-K-Mo₂C/γ-Al₂O₃ during RWGS with recycle. CO₂ conversion and CO selectivity are plotted versus recycle ratio for 1 kg of catalyst with a constant fresh feed flow rate of 60 SLPM and GHSVs over the catalyst from 1.7 L kg⁻¹ s⁻¹ to 5.1 L kg⁻¹ s⁻¹. Single pass equilibrium conversion for these reaction conditions is plotted as a dotted red line. All reactor studies are for a 3:1 H₂:CO₂ reactant ratio at 450 °C and 2.1 MPa.

the recycle ratio increases to 2, the CO:CO₂ ratio within the reactor also increases from 0.8 to 3, resulting in high CO coverage on the catalyst surface.

These results agree with the DFT calculations of adsorbates over oxygen-modified Mo₂C, where CO binds much more strongly (-38 kcal mol⁻¹ at 1 ML) than CO₂ (-7 kcal mol⁻¹ at 1 ML),

resulting in hydrogenation of CO to CH₄, which is observed in Figure 8 with the gradual decrease in CO selectivity from 98.2% to 92.1%. An example of the adsorption configurations for both the clean and O-covered Mo₂C is included as Figure S10 of the Supporting Information.

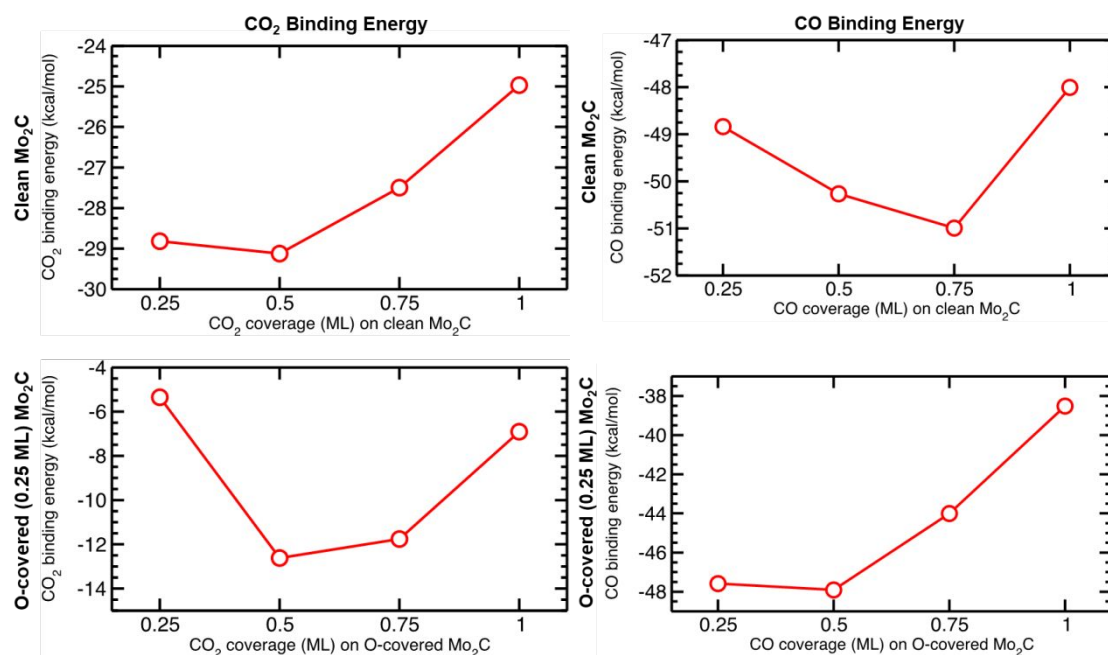


Figure 8. DFT calculations displaying CO₂ and CO adsorption energies for clean Mo₂C and O-covered (0.25 ML) Mo₂C as a function of CO₂ and CO coverage.

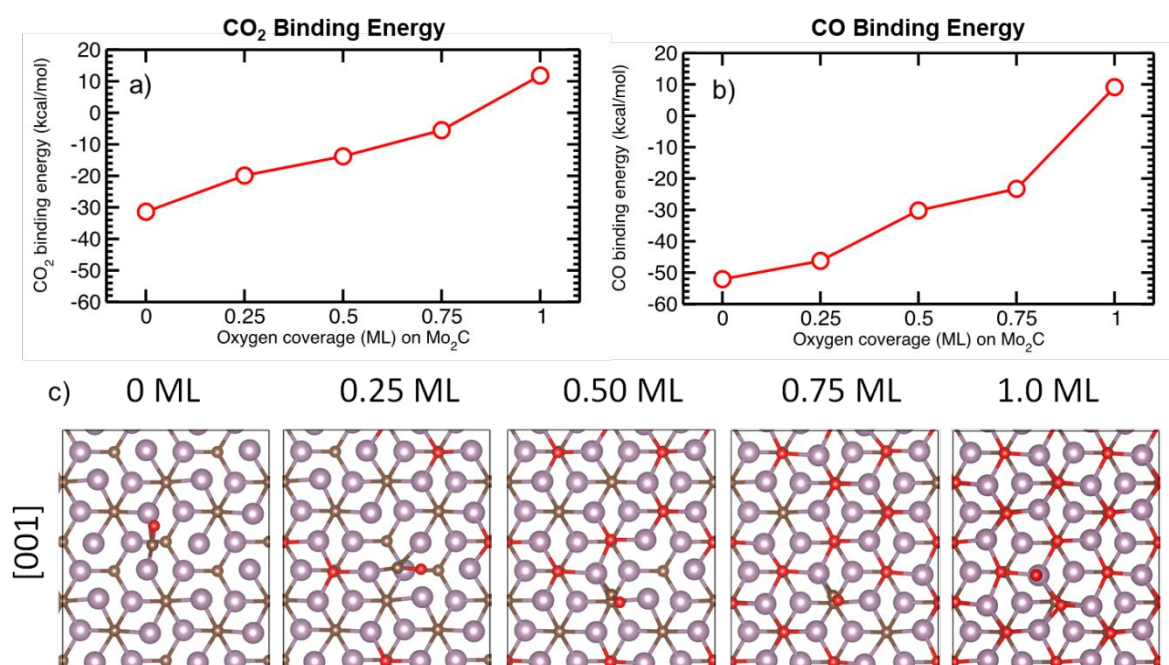


Figure 9. Binding energies of single a) CO₂; and b) CO molecules as a function of oxygen coverage on the Mo-terminated Mo₂C surface; c) Adsorption configurations of CO on the Mo-terminated Mo₂C surface with oxygen coverage ranging from 0 ML to 1.0 ML, viewed along the [001] crystal axis. Binding is endothermic for oxygen coverage larger than 0.75 ML for both CO and CO₂ molecules. CO₂ adsorption data is reproduced from Ref. 55.

X-ray Photoelectron Spectroscopy

To gain additional insight into the active phase of K-Mo₂C/γ-Al₂O₃ that results in high performance for RWGS, X-ray photoelectron spectroscopy (XPS) measurements of the Mo3d, C1s and O1s electrons are conducted for the lab-scale and pilot-scale K-Mo₂C/γ-Al₂O₃. The high stability of P-K-Mo₂C/γ-Al₂O₃ at 300 °C and 450 °C, but transient behavior at 600 °C, suggests that the active phase of the catalyst could be dynamic under the high temperature conditions.

The quantitative ex-situ Mo3d composition of each catalyst from XPS deconvolution can be found in Figure 10 and Table 2, with values of binding energy for each Mo species taken from Oshikawa et. al.⁵⁶ From examining the Mo oxidation state composition before and after the pilot-scale reaction at each temperature, it is clear that during reaction, the metallic Mo phase of the catalyst surface becomes oxidized to contribute to an increase in MoO₃ (Mo⁶⁺). Additionally, within the pilot-scale P-K-Mo₂C/γ-Al₂O₃ catalyst, the Mo⁴⁺ composition, which represents MoO₂, is relatively unchanged after the reaction at 300 °C and 450 °C. These findings generally support the observations of the XRD patterns shown in Figure 3, where significant changes to the bulk crystalline structure of the catalyst do not occur during reaction.

The exception is at 600 °C, where XRD in Figure 3 indicates no significant deformations to bulk crystalline structure, yet the XPS spectra of the Mo3d electron exhibits significant increases to the Mo⁶⁺ contribution, with a corresponding decrease to Mo⁴⁺. Careful inspection of the data in Figure 10 shows much lower counts per second for the spent catalyst at 600 °C versus the other samples, suggesting coking of the active Mo phase at 600 °C, which is further supported by the high C1s counts in Figure 11. Additionally, as shown in the deconvoluted XPS quantification in Table 2, the decrease in Mo⁴⁺ composition at 600 °C is accompanied by a corresponding increase to Mo⁶⁺, indicating that MoO₂ is further oxidized during reaction, likely

causing the decrease in CO selectivity at 600 °C observed in Figure 5, due to the electronic modification of Mo sites by oxygen that results in the dramatically different adsorption behavior of CO versus CO₂ as described in the DFT calculations in Figures 8 and 9.⁵⁵

Table 2. Composition of deconvoluted XPS spectra for K-Mo₂C/γ-Al₂O₃ before and after laboratory-scale RWGS reaction at 300 °C, 450 °C and 600 °C at a GHSV of 1.7 L kg⁻¹ s⁻¹ for a 3:1 H₂:CO₂ ratio at 2.1 MPa.

Catalyst	Mo ⁰	Mo ²⁺	Mo ⁴⁺	Mo ⁶⁺
L-K-Mo ₂ C As-Synthesized	6.6	14.8	39.5	39.0
P-K-Mo ₂ C As-Synthesized	13.8	14.9	56.9	14.5
P-K-Mo ₂ C 300 °C Post-Reaction	13.9	6.8	64.8	14.5
P-K-Mo ₂ C 450 °C Post-Reaction	10.9	4.4	77.0	7.7
P-K-Mo ₂ C 600 °C Post-Reaction	2.0	7.0	46.9	44.1

This XPS characterization supports previous conclusions emphasizing the dynamic oxidation state of Mo₂C-based catalysts under reaction conditions.⁴¹ Additional deconvolution of XPS spectra for the as-synthesized P-K-Mo₂C/γ-Al₂O₃ and L-K-Mo₂C/γ-Al₂O₃ are found in Figures S11, S12 and Table S3 of the Supporting Information.

To further investigate trends between catalytic structure and performance, analysis of the C1s XPS spectra of the as-synthesized and spent catalysts is shown in Figure 11. Formation of the active carbide phase can be assigned to a C-Mo peak at 283.3 eV.⁵⁶ For the pilot-scale catalyst before and after reaction at 300 °C, a C-Mo shoulder cannot be clearly identified in Figure 11. The C-Mo shoulder could be enveloped by the graphitic carbon peak, or the XPS spectra is providing further evidence that carburization of P-K-Mo₂C/γ-Al₂O₃ is incomplete, which is supported by the XRD spectra in Figure 3. The peaks at higher binding energies can be attributed to the K2p signal of potassium, present within the K-Mo₂C catalyst.⁵⁷ As observed in the spectra, this signal between 290-295 eV

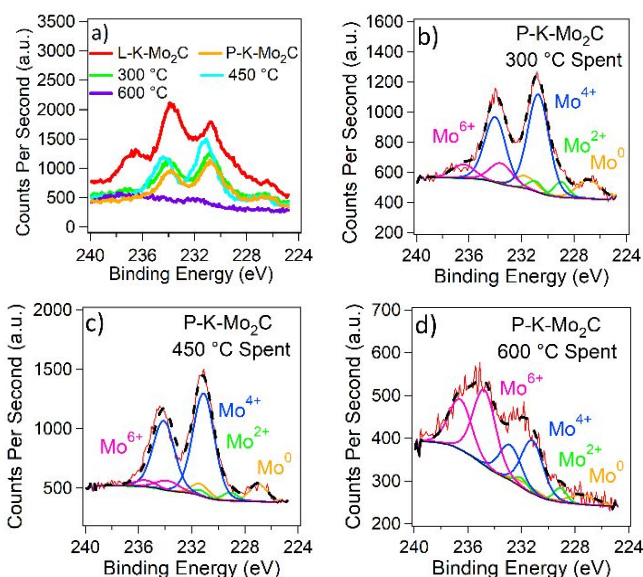


Figure 10. a) Mo3d spectra of as-synthesized L-K-Mo₂C/γ-Al₂O₃ and P-K-Mo₂C/γ-Al₂O₃ (dashed black lines), with spectra included of P-K-Mo₂C/γ-Al₂O₃ after laboratory-scale reaction at 300 °C, 450 °C and 600 °C. Deconvoluted Mo3d spectra (solid line) of P-K-Mo₂C/γ-Al₂O₃ with fits (dashed line) after 12 h on stream at b) 300 °C; c) 450 °C; and d) 600 °C. Contributions include Mo⁶⁺, Mo⁴⁺, Mo²⁺ and Mo⁰.

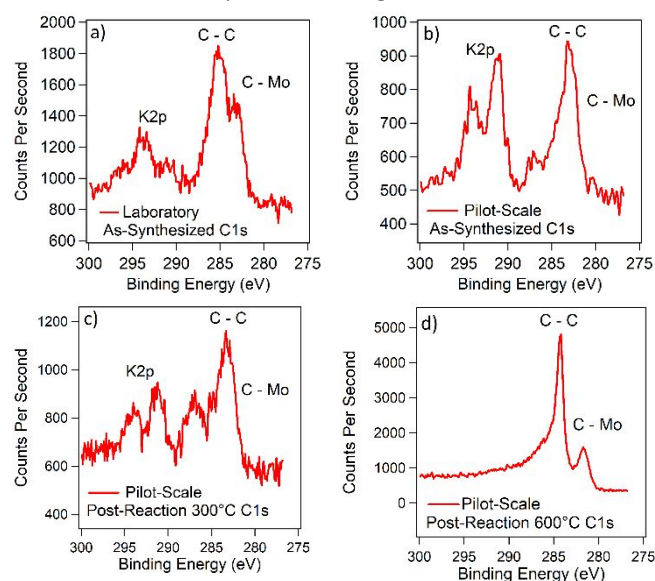


Figure 11. C1s XPS spectra for a) as-synthesized L-K-Mo₂C/γ-Al₂O₃; b) as-synthesized P-K-Mo₂C; c) P-K-Mo₂C/γ-Al₂O₃ after reaction at 300 °C; and d) P-K-Mo₂C/γ-Al₂O₃ after reaction at 600 °C. XPS spectra are recorded ex-situ after 12 h on stream in the laboratory with 3:1 H₂:CO₂ ratio at 2.1 MPa.

remains relatively constant as compared to the graphitic carbon peak, both before and after reaction at 300 °C, suggesting minimal coking of the catalyst surface under these reaction conditions.⁵⁸ However, for P-K-Mo₂C/γ-Al₂O₃ reacted at 600 °C, the C-C peak dominates the spectra, indicating that the surface of the catalyst becomes covered in coke at the high temperature reaction conditions, potentially leading to the transient catalyst behavior, and in turn, the CH₄ formation observed during reactor studies.⁵⁸

Analysis of the O1s XPS spectra of the as-synthesized and spent catalysts (Figure S13 of the Supporting Information) shows formation of a distinct O-Mo peak at 531 eV for all catalysts. The O-Mo peak could be characteristic of an oxycarbide, the active phase for RWGS.⁵⁴ The P-K-Mo₂C/γ-Al₂O₃ catalyst after laboratory-scale reaction 600 °C displays an additional oxide peak associated with carbonate species at ~536 eV, which provides evidence that oxidation is attributing to the increase in CH₄ selectivity, as carbonate species are common intermediates during CO₂ methanation.^{58, 59} At temperatures of 600 °C, carburization begins over Mo-based catalysts, which suggests a dynamic surface structure and limited catalyst stability under these high temperature conditions, despite unchanged bulk structure as evidenced by the XRD patterns in Figure 3.⁵⁸

Pulse Chemisorption and Temperature Programmed Desorption

To gain a better understanding of the relationship between reactor performance and catalyst structure, N₂ physisorption according to BET method of the P-K-Mo₂C/γ-Al₂O₃ catalyst before and after reaction is shown in Table 3. As shown in the table, there is a decrease in N₂ physisorption according to BET method after reaction. Although there is little change observed in the textural properties of the catalyst during RWGS, pulse chemisorption of the CO₂ reactant and CO product can provide further insight into the dynamic changes in catalyst structure observed in the XPS data.

As shown in Table 3, we also observe a much larger amount of CO₂ adsorbed relative to CO for the as-synthesized P-K-Mo₂C/γ-Al₂O₃, which is favorable for high CO selectivity during RWGS. This is likely from the large surface concentration of potassium seen in the C1s XPS in Figure 11b, which provides basic sites that are favorable for CO₂ adsorption prior to reaction. However, for all catalysts after reaction, there is an order of magnitude decrease of chemisorbed CO₂, combined with a corresponding increase in adsorbed CO. The decrease of

chemisorbed CO₂ on K-Mo₂C could be due to surface oxidation that occurs during CO₂ dissociation,^{28, 53} decrease in surface K, as shown by XPS in Figure 11, and/or coking that occurs during reaction. If the surface of the catalyst becomes oxidized, this likely leads to a more pronounced decrease in CO₂ coverage relative to CO, supported by the aforementioned DFT calculations in Figures 8 and 9. Additionally, coke formation would significantly decrease the affinity of the catalyst to CO₂, as suggested by DFT calculations in Figure S14, revealing weak binding of CO₂ (-1.06 kcal mol⁻¹) on C-terminated Mo₂C. This behavior is consistent with the decrease in CO₂ coverage after reaction.

To further probe the adsorption behavior of CO₂, temperature programmed desorption (TPD) experiments are shown in Figure 12. When examining the relative binding strength of CO₂ over the as-synthesized and P-K-Mo₂C/γ-Al₂O₃ reacted at 300 °C, 450 °C and 600 °C, the overall shape of the TPD profiles are fairly similar with a few exceptions. Each profile generally contains a broad desorption peak at ~400 °C, while the peak for the as-synthesized catalyst is shifted toward a higher temperature. For the CO-TPD (Supporting Information, Figure S15), similar desorption behavior is observed as the CO₂-TPD profile in Figure 12, suggesting that CO₂ and CO adsorb on the same active sites over K-Mo₂C/γ-Al₂O₃.

A significant exception is the CO₂-TPD profile for P-K-Mo₂C/γ-Al₂O₃ after reaction at 450 °C, which is both broader and larger than the TPD profiles of the other conditions. These data suggest that the high performance observed in the reactor at 450 °C could be a result of either: (1) Improved dissociation of adsorbed CO₂ into CO; or (2) Rapid CO₂ and CO adsorption/desorption, potentially minimizing any desorption limitations on the reaction kinetics.

For the 600 °C trial, the decrease in CO selectivity and corresponding increase in CH₄ selectivity (Figure 5) is correlated with a relative decrease in intensity of the peak at 450 °C. This could suggest that CO₂ and CO exhibit stronger adsorption over the P-K-Mo₂C/γ-Al₂O₃ reacted at 600 °C, which results in a net increase in the rate of CO hydrogenation to CH₄, and in turn, higher CH₄ selectivity. It is important to note, however, that the TPD experiments are measuring the composition of the effluent gas with a thermal conductivity detector (TCD), so we performed additional experiments to test for decomposition of the catalyst. These experiments are particularly important, because large peaks are observed during the TPD experiments at high temperature ~700 °C in Figure S16.

Table 3. N₂ physisorption and CO₂ and CO chemisorption over Mo₂C/γ-Al₂O₃ as-synthesized and after laboratory-scale reaction at 300 °C, 450 °C and 600 °C.

P-K-Mo ₂ C Condition	N ₂ Physisorption According to BET Method (m ² g ⁻¹)	Total Pore Volume by N ₂ Physisorption (cm ³ g ⁻¹)	CO ₂ Quantity Adsorbed (μmol g ⁻¹)	CO Quantity Adsorbed (μmol g ⁻¹)
As-Synthesized	142	0.6	29.5	0.2
300 °C Post-Reaction	138	0.6	4.3	1.2
450 °C Post-Reaction	115	0.5	1.1	1.0
600 °C Post-Reaction	120	0.6	2.7	1.7

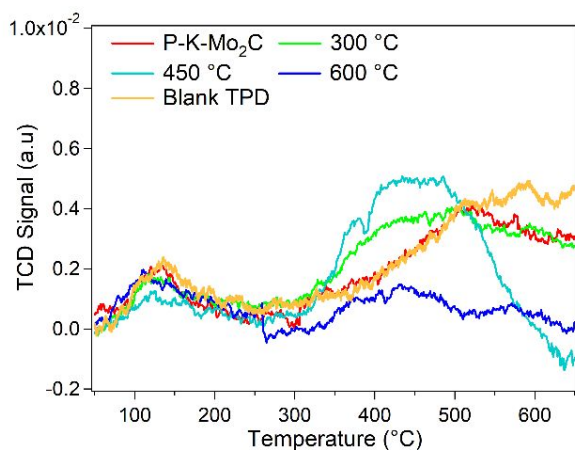


Figure 12. CO₂-TPD for as-synthesized (red) and spent P-K-Mo₂C/γ-Al₂O₃ after 12 h on stream at 300°C (green), 450°C (teal) and 600 °C (blue) from 100 °C to 650 °C with a ramp rate of 5 °C min⁻¹.

To understand if there is any significant catalyst decomposition that would affect the reaction, Figure S17a shows the Mo K-edge X-ray absorption near-edge structure (XANES) spectra of the P-K-Mo₂C catalyst as-synthesized and after reduction. Careful examination of the Mo K-edge XANES in Figure S17a shows a slight shift of the first peak located at approximately 20010 eV toward lower energies, which is associated with partial reduction of the MoO₃ passivation layer after reduction. More importantly, when comparing the reduced catalyst with the catalyst after reaction at 450 °C and 600 °C in Figure S17b, it is clear that all catalysts are relatively stable during the reaction. When combined with the reactor data and CO₂ and CO TPDs in Figures 12 and S15, respectively, these XANES data provide further support that the catalyst is stable and not decomposing during reaction.

Discussion

As shown in the results section, P-K-Mo₂C/γ-Al₂O₃ exhibits high performance for the RWGS reaction at both the laboratory and pilot-scales, with minimal deactivation and >95% CO selectivity under most reaction conditions. In assessing the viability for scale-up, there is a reported difference between the range of GHSVs tested at each scale. Clearly, P-K-Mo₂C/γ-Al₂O₃ under pilot-scale conditions is equilibrium and/or mass-transfer limited because reactant flow rates above 200 SLPM could not be achieved, but higher GHSVs (36.7 L kg⁻¹ s⁻¹) have been measured in the laboratory to test catalytic stability in the kinetically limited regime. Nevertheless, there is good agreement between the laboratory and pilot-scale reactor data, providing strong evidence that the P-K-Mo₂C/γ-Al₂O₃ catalyst has high potential for scale-up as part of an industrial CO₂ hydrogenation process. It is important to note, however, that there are distinct differences between the K-Mo₂C/γ-Al₂O₃ catalyst synthesized on the laboratory and pilot-scales. This is illustrated in the reactor data in Table 4, where P-K-Mo₂C/γ-Al₂O₃ exhibits improved performance, illustrated by the ~25% higher CO STY, relative to what has been previously reported for L-K-Mo₂C/γ-Al₂O₃ under analogous reaction conditions,⁴¹

requiring further characterization to understand the cause of this discrepancy.

The difference in catalytic performance can be explained by the differences in bulk crystalline structure observed between the pilot and laboratory-scale catalysts, which is a result of slight differences in catalyst synthesis, outlined in the experimental section. In brief, for P-K-Mo₂C/γ-Al₂O₃, the molybdenum and potassium precursors are introduced into the γ-Al₂O₃ trilobe support from St. Gobain via three-step incipient wetness impregnation with a molar ratio of 1/4/15 K/Mo/γ-Al₂O₃. After impregnation, the catalyst is calcined, carburized for 4 h at 660 °C and passivated.

The laboratory-scale synthesis procedure is similar, but the γ-Al₂O₃ is a powder sourced from Alfa Aesar and the catalyst is carburized for 5 h at 600 °C. Another key distinction between these synthesis procedures is the batch size of the final Mo₂C-based catalyst. The pilot-scale procedure results in a yield of ~3 kg of catalyst, while the laboratory-scale synthesis yields ~3 g. Although the overall procedures are mostly analogous, it is likely that heat and/or mass transfer differences during pilot-scale carburization result in the incomplete carburization of P-K-Mo₂C, observed in the XRD in Figure 3 and XPS in Figures 10 and 11.

To address the discrepancy in carburization conditions, we performed additional experiments where we calcined the P-K-Mo₂C (350 °C for 6 h), then recarburized the catalyst under laboratory-scale conditions (LC-P-Mo₂C) to understand if the scaled-up carburization affects RWGS performance. The XRD and XPS of the recarburized catalyst has been added to the Supporting Information (Figures S18 and S19). We also performed reactor studies over the recarburized catalyst at 450 °C, which have been added to Table 4 and labeled as LC-P-Mo₂C.

As seen in Table 4, LC-P-Mo₂C is even more active than our original P-K-Mo₂C catalyst, indicating the performance of K-Mo₂C is very sensitive to the carburization conditions. The difference in performance can likely be attributed to the structure of each catalyst, where XRD and XPS in Figures S18 and S19 respectively, show the primary phase of LC-P-Mo₂C is Mo₂C with some surface oxides. The bulk structure of the resynthesized LC-P-Mo₂C, shown by XRD in Figure S18 is similar to that of L-K-Mo₂C, but the XPS in Figure S19 shows distinctly more surface carbide and less MoO₃ in LC-P-Mo₂C versus L-K-Mo₂C. Together, these data further suggest that an oxycarbide is the active phase for RWGS, agreeing with previous studies over Mo₂C-based catalysts.^{30, 41 30, 41 30, 41}

There is also a higher potassium to carbon ratio in P-K-Mo₂C/γ-Al₂O₃ when compared to L-K-Mo₂C/γ-Al₂O₃, as observed in the C1s XPS spectra in Figure 11, although the precursor ratios are kept the same during synthesis of the laboratory and pilot-scale catalysts. As observed in Figure S19 of the Supporting Information, the C1s XPS signal of LC-P-Mo₂C is much weaker than that of P-K-Mo₂C, with similar potassium to carbon ratios as P-K-Mo₂C. However, as mentioned previously, this may be due to an Mo₂C phase segregating to the surface of LC-P-Mo₂C during recarburization.

The slight differences between the laboratory and pilot-scale catalysts translate to a measurable difference in catalytic

performance, illustrated by the ~25% higher CO STY of the pilot-scale catalyst at 450 °C and a GHSV of 36.7 L kg⁻¹ s⁻¹ in Table 4. Arrhenius experiments on both catalysts also agree with these findings, showing apparent activation energies of 16.3 kcal mol⁻¹ and 22.5 kcal mol⁻¹ for P-K-Mo₂C and L-K-Mo₂C, respectively. The Arrhenius plot can be found in Figure S20 of the Supporting Information.

In fact, the performance of P-K-Mo₂C/γ-Al₂O₃ for RWGS at 450 °C in Figure 1 outperforms all other RWGS catalysts reported in literature under similar conditions when accounting for the cost and production rate of CO. Additionally, benchmarks are included for Cu-ZnO/Al₂O₃ and FeCrO_x, the low and high temperature water-gas shift (WGS) catalysts, respectively. When accounting for CO yield and cost of the active phases of the catalysts, it is clear that K-Mo₂C/γ-Al₂O₃ has industrial viability for the RWGS reaction, especially at 450 °C.

However, the Fe and Cu catalysts supported on CeO₂ in Figure 1 and Table 4 perform better than P-K-Mo₂C/γ-Al₂O₃ according to certain metrics (\$ metal kg CO⁻¹). It is important to note that the high performance of these transition metal catalysts are partially from the higher H₂:CO₂ ratio (4:1), which results in an equilibrium conversion at 400 °C of 41.3% versus 36.7% for a 3:1 H₂:CO₂ ratio.^{25, 34, 60} These studies by Dai et al. are also performed at atmospheric pressure, which provides proof-of-concept for catalytic activity and selectivity, however, it is also necessary to operate catalysts at more relevant industrial conditions to examine the catalyst scalability.⁶¹ For P-K-Mo₂C, we have included measurements at atmospheric pressure (0.1 MPa) as references in Figure 1 and Table 4, which result in lower conversion and CO selectivity than the analogous experiment at high pressure (2.1 MPa).

Although P-K-Mo₂C/γ-Al₂O₃ is a high-performance catalyst at 450 °C, at 600 °C the CO selectivity rapidly declines with time-on-stream, as detailed in Figure 5. The catalyst after the time-on-stream trial at 600 °C was collected, reduced and run under analogous reaction conditions and noted in Table 4 as "Revitalized". Within this trial, the CO selectivity did not recover to the initial value during the first 14 h on-stream in Figure 5. Additionally, the XRD patterns collected after RWGS at 300 °C and 600 °C in Figure 3 suggest that the bulk structure of the catalyst is unchanged at both temperatures, but the significant decrease in CO selectivity suggests the active phase of the catalyst is transient at 600 °C.

From the XPS data and chemisorption data of CO₂ and CO after reaction at 600 °C, the catalytic surface likely becomes coked and oxidized. The coking is evidenced by the high C1s counts at 600 °C relative to the catalyst reacted at lower temperatures. Oxidation of the surface can be inferred by the decrease in CO₂ adsorption and corresponding increase in CO adsorption after reaction at 600 °C (Table 3), when combined with the DFT calculations, which show that oxygen-modified Mo₂C binds CO much more strongly than CO₂ (Figure 8).

Furthermore, additional DFT calculations of CO and CO₂ binding at higher coverage (Figure 9) indicate that oxygen coverage likely does not exceed 0.75 ML, since both CO and CO₂ binding is endothermic at high coverage, while experiments show that the catalyst remains active. Moreover, our

calculations demonstrate that CO consistently binds more strongly than CO₂ at oxygen coverage up to and including 0.75 ML on the Mo-terminated surface. Calculations on the C-terminated Mo₂C, found in Figure S14 of the Supporting Information, indicate that neither CO nor CO₂ adsorb.

Together, these data suggest that coking and oxidation of the catalytic surface cause weaker binding of CO₂ relative to CO, resulting in higher surface coverage of CO and subsequent hydrogenation to CH₄, the undesired product. As an alternative mechanism, the coke accumulating on the catalyst surface could be subsequently hydrogenated to CH₄, similar to processes used to remove coke from the surface of catalysts during carburization.⁶²

An increase in CH₄ selectivity is also observed during the recycle experiments at higher recycle ratios in Figure 7. When evaluating the scale-up viability of K-Mo₂C/γ-Al₂O₃, it is important to assess if the increase in CO yield at higher recycle ratios is worth the expense of decreased CO selectivity. If the desired products are C₆+ hydrocarbons, then every mole of CH₄ produced within the RWGS reactor is a waste of energy and valuable H₂. Depending on the exact application of the catalyst and process, it is possible a more moderate recycle ratio of 1 is desired, which results in a CO₂ conversion of 71% with a CO selectivity approaching 95%. This result is arguably better than the single pass conversion of 48.1% with a CO selectivity of 98.2%, because in a two-reactor CO₂-FT process, unreacted CO₂ will likely be hydrogenated to methane in the downstream FT reactor.⁶³ Nevertheless, the performance of K-Mo₂C/γ-Al₂O₃ at 450 °C is arguably better than any other catalyst tested under similar conditions. With the low-cost of Mo, K and Al₂O₃, the industrial viability is clear, and K-Mo₂C/γ-Al₂O₃ should be further tested and explored for scale-up.

Industrial Deployment

The first step of industrial scale conversion of CO₂ is sourcing CO₂ either directly from effluent flue gases or through atmospheric carbon capture processes.⁹ Depending on the CO₂ and H₂ source, industrial CO₂ utilization can have significant impacts on the chemical and energy supply chains.⁶⁴ To compare the cost associated with different types of CO₂ utilization technologies, the price equivalent of converted CO₂ to one gallon of gasoline (gge) is a useful metric.

One study by Stechel et al. indicates that the cost of using CO₂ via flue gas or direct air capture would contribute \$0.35 gge⁻¹ to \$5.34 gge⁻¹, without accounting for the cost of hydrogen.⁶⁵ The estimated cost of production for a gallon of liquid fuel from CO₂ and H₂ is \$4.14 gge⁻¹,⁶⁶ not including estimated capture costs, bringing a combined fuel cost potentially as high as \$9.48 gge⁻¹, far from a cost-competitive price when compared to traditional petrochemical production.

These rough estimates on the feasibility of CO₂ utilization can give some insight into the overall economic feasibility of the process, showing that advancements in lowering the cost of CO₂ and H₂ are both necessary. However, determination of inherent scalability is imperative for effective catalytic development and can be researched in parallel to improved carbon capture and H₂ production technologies.⁷³⁻⁷⁵

As such, there is a need to benchmark the performance of RWGS catalysts and determine suitability for incorporation into a CO₂ utilization process.⁶⁷⁻⁷¹ The authors have proposed two metrics to directly compare and evaluate different catalysts for scale-up. These metrics are CO production rate (kg CO kg metal⁻¹ day⁻¹) and material cost of CO (\$ metal kg CO⁻¹). The current work shows that P-K-Mo₂C/γ-Al₂O₃ is a top performing catalyst for both of the above metrics (found closest to the top right of Figure 1), indicating that P-K-Mo₂C meets the challenge of developing a highly stable RWGS catalyst with high CO selectivity that translates to the pilot-scale.⁷² With further development of CO₂ capture technologies,⁷⁶ CO₂ utilization could become an environmentally friendly and economically competitive process compared to traditional liquid fuel production.

Although not yet economically competitive with fossil-fuel sourced hydrocarbon production, NRL is developing a proof of concept system capable of producing up to four liters of liquid hydrocarbon fuel per day from seawater as part of a project to provide fuel for the Navy at sea. The overall system consists of three modular skids: (1) An electrolytic cation exchange module (E-CEM), which can process 135,000 L of seawater per day (94 L min⁻¹) to produce 21,000 L of H₂ (14.5 L min⁻¹) and 7,000 L of CO₂ (4.9 L min⁻¹); (2) A gas collection and storage skid, to dry, compress and store the H₂ and CO₂ produced by the E-CEM; and (3) A fuel synthesis skid, containing RWGS and FT reactors.⁷⁷⁻⁷⁹ The design of each skid and a general process flow diagram for the system can be found in Figure 13. After demonstrating the viability of P-K-Mo₂C for pilot-scale RWGS, the next step is to integrate the three modules together and demonstrate proof of concept for the overall seawater-to-fuel system. Although the capacity of the system is an insignificant fraction of the total fuel usage of the US Department of Defense (48 million L day⁻¹), the development of the modular system is an important step toward deployment at an industrially relevant scale.⁸⁰

There are also future plans to capture and convert effluent CO₂ from power plants, a research and development goal of the US Department of Energy.⁸¹ Extending P-K-Mo₂C from CO₂ derived from seawater to CO₂ captured from flue gas of coal fired power plants requires that the stability of P-K-Mo₂C is tested when exposed to common contaminants such as mercury, sulfur, cadmium and chlorine.^{82, 83} The overall industrial utility of P-K-Mo₂C as a RWGS catalyst will ultimately depend if the high stability under pure CO₂ and H₂ can be extended to an inlet gas stream containing traces of contaminants that are the subject of future studies.

Perhaps the most promising aspect of the P-K-Mo₂C catalyst is the high CO STY at industrially relevant pressures (~2 MPa). There is a need for more RWGS studies over low-cost transition metal catalysts under industrially relevant conditions.⁶¹ In the current work, we have addressed this need, and as shown in Figure 1 and Table 4, the overall performance of K-Mo₂C and

cost of CO at 450 °C is unmatched by the current state-of-the-art. Operating the catalyst at elevated pressures allows the effluent gas from the RWGS reactor to be fed directly into a downstream FT or methanol synthesis reactor. The challenge of FT is that unreacted CO₂ after RWGS can be converted into undesirable CH₄ over typical FT catalysts.¹⁶ With a recycle stream and further process optimization, we can react the majority of CO₂ under milder conditions when compared to the very high temperatures (~800 °C) required for full conversion.

Another option is to integrate the RWGS catalyst with a FT active phase for a CO₂-FT tandem catalyst. Although such tandem catalysts are difficult to design, the distinct advantages of operating CO₂-FT over a tandem catalyst or dual-bed configuration are: (1) CO₂-FT is an exothermic reaction, and as a result, the heat evolved from FT can be used to supply energy to the endothermic RWGS, increasing the thermal efficiency of the overall process above the ~38% for stand-alone RWGS;^{8, 84} and (2) Higher CO₂ conversion can be achieved by using a sufficiently fast FT catalyst to rapidly consume CO to drive the reaction equilibrium toward hydrocarbon products via Le'Chatelier's principle. Overcoming equilibrium limitations of thermally-driven CO₂ hydrogenation reactions without recycling unconverted species has been recognized as a significant challenge for industrial deployment.⁸⁵ However, as we have shown here, the P-K-Mo₂C catalyst is stable and produces CO with high selectivity up to a recycle ratio of two.

If methanol is desired as a final product instead of CO, it may not be necessary to run RWGS with multi-pass conversion, increasing the utility of our P-K-Mo₂C catalyst. Under the pilot-scale operating conditions with recycle in Figure 7, the effluent CO:CO₂ ratio is ~0.8 with a stoichiometric number of $M = 2$ ($M = \frac{MH_2 - MCO_2}{MCO + MCO_2}$).^{86, 87} Upon the addition of additional H₂ (1 mol per mol of effluent CO) the effluent gas composition can be brought within the typical range for methanol synthesis.⁸⁸ Additionally, because we are running the RWGS reaction under higher pressures (2.1 MPa), after water and heat removal, the effluent from our pilot reactor requires less pressurization for downstream methanol synthesis (P = 5-15 MPa) relative to other RWGS studies (0.1 MPa).

Industrial deployment of the RWGS reaction as part of a cyclical economy to utilize CO₂ as a carbon source for the above examples requires a source of renewable and CO₂-free H₂. Currently, the vast majority (ca. 90%) of H₂ is produced from either steam reforming of CH₄ or coal gasification, resulting in significant CO₂ emissions.¹⁴ For industrial viability, and to produce fuel that is cost competitive with gasoline, estimates show that the cost of renewable H₂ must be reduced to between \$2.60 to \$3.00 kg⁻¹.^{89, 90} As mentioned above, NRL has developed a process for co-generation of H₂ and CO₂ from seawater, which if deployed on a large enough scale, can also mitigate the negative effects associated with ocean acidification that cannot be resolved by direct air capture.⁹¹



Figure 13. US Naval Research Laboratory modular seawater-to-fuel system consisting of an electrolytic cation exchange module (E-CEM), gas collection and storage skid and fuel synthesis skid. The pilot-scale system can produce up to four liters of jet fuel per day (2.8 mL min^{-1}).

Table 4. Comparison of P-K-Mo₂C/γ-Al₂O₃ with other high-performance RWGS catalysts at varying conditions for benchmarking catalytic performance. The asterisk (*) indicates this work. The P-K-Mo₂C/γ-Al₂O₃ trial marked with (†) has been conducted with the pilot-scale reactor. All other reaction trials marked with an asterisk (*) have been performed using the laboratory-scale reactor. (‡) The Argus Metals database was utilized to obtain active metal costs on a per gram basis for the CO Cost (\$ metal kg CO⁻¹) calculation. Further details regarding the reaction conditions are included within the experimental section. For catalysts with greater than 2% of carbon as C₃₊ products, a detailed distribution of products is provided in the Supporting Information in Table S4 and additional catalysts for benchmarking are included in Table S5. In all cases, no oxygenates are detected.

Catalyst	T (°C)	P (MPa)	H ₂ :CO ₂ Ratio	GHSV (L kg ⁻¹ s ⁻¹)	Conversion (%)	Carbon-based Selectivity (%)				CO Yield (%)	CO STY (μmol CO gcat ⁻¹ s ⁻¹)	CO Production Rate (kg CO produced day ⁻¹ kg metal ⁻¹)	CO Cost (\$ metal kg CO ⁻¹)
						CO	CH ₄	C ₂ H ₆ and C ₂ H ₄	C ₃₊				
*L-K-Mo ₂ C/γ-Al ₂ O ₃	450	2.1	3	36.7	22.1	97.3	2.0	0.7	0.0	21.5	80.0	984.2	0.02
*P-K-Mo ₂ C/γ-Al ₂ O ₃	450	2.1	3	36.7	26.8	99.3	0.3	0.4	0.0	26.6	99.1	1219.0	0.02
*LC-P-Mo ₂ C/γ-Al ₂ O ₃	450	2.1	3	36.7	42.7	99.1	0.6	0.3	0.0	42.4	157.7	1940.1	0.01
*P-K-Mo ₂ C/γ-Al ₂ O ₃	450	2.1	3	18.3	33.1	99.88	0.09	0.03	0.0	33.0	61.4	755.6	0.03
*P-K-Mo ₂ C/γ-Al ₂ O ₃	450	2.1	3	1.8	42.1	99.1	0.8	0.2	0.2	41.7	7.8	95.5	0.22
†P-K-Mo ₂ C/γ-Al ₂ O ₃	450	2.1	3	1.7	48	98.9	1.1	0.0	0.0	47.5	8.8	97.8	0.20
*P-K-Mo ₂ C/γ-Al ₂ O ₃	450	0.1	3	1.8	21.1	93.3	6.0	0.7	0.0	19.7	3.7	45.1	0.47
*P-K-Mo ₂ C/γ-Al ₂ O ₃	600	2.1	3	3.7	59.0	98.1	1.8	0.1	0.0	57.9	21.5	265.0	0.08
*Revitalized P-K-Mo ₂ C/γ-Al ₂ O ₃	600	2.1	3	3.7	58.7	43.2	52.1	4.0	0.7	25.4	9.4	116.2	0.18
*P-K-Mo ₂ C/γ-Al ₂ O ₃	300	2.1	3	36.7	1.2	99.2	0.8	0.0	0.0	1.2	4.3	52.9	0.40
*Cu-ZnO/Al ₂ O ₃	300	2.1	3	36.7	23.3	92.6	4.6	2.8	0.0	21.6	80.2	194.0	0.03
*FeCrO _x	450	2.1	3	36.7	47.5	48.6	37.3	7.3	6.8	23.1	85.8	207.7	0.0001
Rh/S-1 ²²	450	1	3	3.3	38.0	71.3	28.7	N/A	N/A	27.1	3.0	1828.8	38.28
InNi ₃ C _{0.5} /Al ₂ O ₃ ⁹²	420	1	3	6.0	35.6	88.8	1.0	10.2	N/A	31.6	10.35	30.9	6.91
Pt/TiO ₂ ²³	400	0.1	1	1.7	14.9	100.0	0.0	N/A	N/A	14.9	5.0	1231.5	22.74
Fe/CeO ₂ ²⁵	400	0.1	4	16.7	8.1	100.0	0.0	N/A	N/A	8.7	6.5	208.6	0.00009
Cu/CeO ₂ ²⁵	400	0.1	4	16.7	31.3	100.0	0.0	N/A	N/A	31.3	23.3	667.6	0.008
Fe/TiO ₂ ⁹³	270	2.0	3	2.2	2.7	73.0	11.6	5.1	10.3	1.9	0.96	92.9	0.0002

Conclusions

K-Mo₂C/γ-Al₂O₃ is a highly active, selective and stable RWGS catalyst at both the laboratory and pilot-scale within the temperature range of 300 to 450 °C. However, at the highest temperature tested of 600 °C, the CO selectivity significantly decreases due to coking and oxidation of the Mo-based active phase of K-Mo₂C/γ-Al₂O₃. This is evidenced by Mo3d, C1s and O1s XPS data, DFT calculations of CO₂ and CO adsorption over Mo₂C and observed decreases in the catalytically active surface area and CO₂ binding strength, via CO₂ pulse chemisorption and CO₂-TPD, respectively. This work demonstrates K-Mo₂C/γ-Al₂O₃ is an effective RWGS catalyst between 300 – 450 °C at a range

of GHSVs, outperforming all other RWGS catalysts reported in literature when accounting for space-time yield of CO and cost of the active phase. Therefore, K-Mo₂C/γ-Al₂O₃ is viable for scale-up as part of a large-scale process for CO₂ hydrogenation to value-added chemicals and fuels.

Conflicts of Interest

There are no conflicts to declare.

Statement of Contributions

MJ prepared the manuscript and performed the laboratory-scale experiments with help from MV. JH and LF supervised and

conducted the pilot-scale experiments. DB and MD performed the DFT calculations and GM supervised the computational tasks of the project. JM and JB facilitated analysis and communication of the data. HW supervised the design, planning and execution of the experiments at NRL. MP conceptualized and coordinated the work and supervised the design, planning and execution of the experiments at the University of Rochester.

Acknowledgements

We acknowledge support from the US Department of Defense, Office of Naval Research, under Award No. N00173-18-P-1439. This research used the 8-ID beamline (ISS) of the National Synchrotron Light Source II, a US Department of Energy (DOE) Office of Science User Facility operated for the DOE Office of Science by Brookhaven National Laboratory under Contract No. DE-SC0012704. DB, MD and GM would like to acknowledge computational support from the Center for Research Computing at the University of Pittsburgh.

References

- S. Saeidi, S. Najari, F. Fazlollahi, M. K. Nikoo, F. Sefidkon, J. J. Klemeš and L. L. Baxter, *Renewable and Sustainable Energy Reviews*, 2017, **80**, 1292-1311.
- J. Ma, N. Sun, X. Zhang, N. Zhao, F. Xiao, W. Wei and Y. Sun, *Catalysis Today*, 2009, **148**, 221-231.
- C. Zhang, K.-W. Jun, K.-S. Ha, Y.-J. Lee and S. C. Kang, *Environ Sci Technol*, 2014, **48**, 8251-8257.
- C. Graves, S. D. Ebbesen, M. Mogensen and K. S. Lackner, *Renewable and Sustainable Energy Reviews*, 2011, **15**, 1-23.
- S. Saeidi, N. A. S. Amin and M. R. Rahimpour, *Journal of CO2 Utilization*, 2014, **5**, 66-81.
- S. C. Peter, *ACS Energy Letters*, 2018, **3**, 1557-1561.
- E. S. Sanz-Pérez, C. R. Murdock, S. A. Didas and C. W. Jones, *Chemical Reviews*, 2016, **116**, 11840-11876.
- Z. Ma and M. D. Porosoff, *ACS Catalysis*, 2019, **9**, 2639-2656.
- D. W. Keith, G. Holmes, D. St. Angelo and K. Heidel, *Joule*, 2018, **2**, 1573-1594.
- G. A. Olah, T. Mathew, A. Goepfert and G. K. Surya Prakash, *Topics in Catalysis*, 2018, **61**, 522-529.
- Y. H. Choi, Y. J. Jang, H. Park, W. Y. Kim, Y. H. Lee, S. H. Choi and J. S. Lee, *Applied Catalysis B: Environmental*, 2017, **202**, 605-610.
- W. Li, H. Wang, X. Jiang, J. Zhu, Z. Liu, X. Guo and C. Song, *Rsc Adv*, 2018, **8**, 7651-7669.
- J. Wei, Q. Ge, R. Yao, Z. Wen, C. Fang, L. Guo, H. Xu and J. Sun, *Nature Communications*, 2017, **8**, 15174.
- G. Centi, E. A. Quadrelli and S. Perathoner, *Energy & Environmental Science*, 2013, **6**, 1711-1731.
- M. K. Gnanamani, G. Jacobs, H. H. Hamdeh, W. D. Shafer, F. Liu, S. D. Hopps, G. A. Thomas and B. H. Davis, *ACS Catalysis*, 2016, **6**, 913-927.
- G. Prieto, *Chemsuschem*, 2017, **10**, 1056-1070.
- Y. A. Daza and J. N. Kuhn, *Rsc Adv*, 2016, **6**, 49675-49691.
- J. A. Rodriguez, P. Liu, X. Wang, W. Wen, J. Hanson, J. Hrbek, M. Pérez and J. Evans, *Catalysis Today*, 2009, **143**, 45-50.
- D. S. Newsome, *Catalysis Reviews*, 1980, **21**, 275-318.
- A. V. Boix, M. a. A. Ulla and J. O. Petunchi, *Journal of Catalysis*, 1996, **162**, 239-249.
- S. Alayoglu, S. K. Beaumont, F. Zheng, V. V. Pushkarev, H. Zheng, V. Iabokov, Z. Liu, J. Guo, N. Kruse and G. A. Somorjai, *Topics in Catalysis*, 2011, **54**, 778.
- C. Wang, E. Guan, L. Wang, X. Chu, Z. Wu, J. Zhang, Z. Yang, Y. Jiang, L. Zhang, X. Meng, B. C. Gates and F.-S. Xiao, *Journal of the American Chemical Society*, 2019, **141**, 8482-8488.
- X. Chen, X. Su, H. Duan, B. Liang, Y. Huang and T. Zhang, *Catalysis Today*, 2017, **281**, 312-318.
- A. Goguet, F. Meunier, J. P. Breen, R. Burch, M. I. Petch and A. Faur Ghenciu, *Journal of Catalysis*, 2004, **226**, 382-392.
- B. Dai, G. Zhou, S. Ge, H. Xie, Z. Jiao, G. Zhang and K. Xiong, *The Canadian Journal of Chemical Engineering*, 2017, **95**, 634-642.
- R. B. Levy and M. Boudart, *Science*, 1973, **181**, 547-549.
- F. Solymosi, A. Oszkó, T. Bánsági and P. Tolmásov, *The Journal of Physical Chemistry B*, 2002, **106**, 9613-9618.
- Y. Shi, Y. Yang, Y.-W. Li and H. Jiao, *Applied Catalysis A: General*, 2016, **524**, 223-236.
- A. A. Koverga, E. Flórez, L. Dorkis and J. A. Rodriguez, *The Journal of Physical Chemistry C*, 2019, **123**, 8871-8883.
- M. D. Porosoff, X. Yang, J. A. Boscoboinik and J. G. Chen, *Angewandte Chemie*, 2014, **126**, 6823-6827.
- M. J. Ledoux, C. P. Huu, J. Guille and H. Dunlop, *Journal of Catalysis*, 1992, **134**, 383-398.
- X. Liu, C. Kunkel, P. Ramírez De La Piscina, N. Homs, F. Viñes and F. Illas, *ACS Catalysis*, 2017, **7**, 4323-4335.
- M. D. Porosoff, S. Kattel, W. Li, P. Liu and J. G. Chen, *Chem Commun*, 2015, **51**, 6988-6991.
- W. Xu, P. J. Ramírez, D. Stacchiola, J. L. Brito and J. A. Rodriguez, *Catalysis Letters*, 2015, **145**, 1365-1373.
- S. Posada-Pérez, F. Viñes, P. J. Ramirez, A. B. Vidal, J. A. Rodriguez and F. Illas, *Physical Chemistry Chemical Physics*, 2014, **16**, 14912-14921.
- M. Xiang, D. Li, J. Zou, W. Li, Y. Sun and X. She, *Journal of Natural Gas Chemistry*, 2010, **19**, 151-155.
- W. D. Mross, *Catalysis Reviews*, 1983, **25**, 591-637.
- D. Li, N. Ichikuni, S. Shimazu and T. Uematsu, *Applied Catalysis A: General*, 1998, **172**, 351-358.
- C. L. O'Young, *The Journal of Physical Chemistry*, 1989, **93**, 2016-2018.
- J. R. Morse, M. Juneau, J. W. Baldwin, M. D. Porosoff and H. D. Willauer, *Journal of CO2 Utilization*, 2019, DOI: 10.1016/j.jcou.2019.08.024.
- M. D. Porosoff, J. W. Baldwin, X. Peng, G. Mpourmpakis and H. D. Willauer, *Chemsuschem*, 2017, **10**, 2408-2415.
- M. E. Dry, *Journal of Molecular Catalysis*, 1982, **17**, 133-144.
- J. Xu, Y. Yang and Y.-W. Li, *Current Opinion in Chemical Engineering*, 2013, **2**, 354-362.
- G. Kresse and J. Furthmüller, *Computational materials science*, 1996, **6**, 15-50.
- M. Dixit, X. Peng, M. D. Porosoff, H. D. Willauer and G. Mpourmpakis, *Catalysis Science & Technology*, 2017, **7**, 5521-5529.

46. M. D. Porosoff, J. W. Baldwin, X. Peng, G. Mpourmpakis and H. D. Willauer, *ChemSusChem*, 2017, **10**, 2408-2415.
47. J. P. Perdew, K. Burke and M. Ernzerhof, *Physical review letters*, 1996, **77**, 3865.
48. M. Methfessel and A. Paxton, *Physical Review B*, 1989, **40**, 3616.
49. E. Parthé and V. Sadogopan, *Acta Crystallographica*, 1963, **16**, 202-205.
50. A. M. Karim, C. Howard, B. Roberts, L. Kovarik, L. Zhang, D. L. King and Y. Wang, *ACS Catalysis*, 2012, **2**, 2387-2394.
51. M. Newville, *J. Synchrot. Radiat.*, 2001, **8**, 322-324.
52. B. Ravel and M. Newville, *J. Synchrot. Radiat.*, 2005, **12**, 537-541.
53. M. D. Porosoff and J. G. Chen, *Journal of Catalysis*, 2013, **301**, 30-37.
54. P. Liu and J. A. Rodriguez, *The Journal of Physical Chemistry B*, 2006, **110**, 19418-19425.
55. M. Dixit, X. Peng, M. D. Porosoff, H. D. Willauer and G. Mpourmpakis, *Catalysis Science & Technology*, 2017, **7**, 5521-5529.
56. K. Oshikawa, M. Nagai and S. Omi, *The Journal of Physical Chemistry B*, 2001, **105**, 9124-9131.
57. S. Selvakumar, N. Nuns, M. Trentesaux, V. S. Batra, J. M. Giraudon and J. F. Lamonier, *Applied Catalysis B: Environmental*, 2018, **223**, 192-200.
58. P. Delporte, F. D. R. Meunier, C. Pham-Huu, P. Vennegues, M. J. Ledoux and J. Guille, *Catalysis Today*, 1995, **23**, 251-267.
59. J. G. Choi and L. T. Thompson, *Applied Surface Science*, 1996, **93**, 143-149.
60. A. Bansode, B. Tidona, P. R. von Rohr and A. Urakawa, *Catalysis Science & Technology*, 2013, **3**, 767-778.
61. E. Schwab, A. Milanov, S. A. Schunk, A. Behrens and N. Schödel, *Chemie Ingenieur Technik*, 2015, **87**, 347-353.
62. Y. C. Kimmel, D. V. Esposito, R. W. Birkmire and J. G. Chen, *International Journal of Hydrogen Energy*, 2012, **37**, 3019-3024.
63. Y. Zhang, G. Jacobs, D. E. Sparks, M. E. Dry and B. H. Davis, *Catalysis Today*, 2002, **71**, 411-418.
64. C. Ampelli, S. Perathoner and G. Centi, *Philosophical Transactions of the Royal Society A: Mathematical, Physical and Engineering Sciences*, 2015, **373**, 20140177.
65. E. B. Stechel and J. E. Miller, *Journal of CO2 Utilization*, 2013, **1**, 28-36.
66. A. Elgowainy, J. Han, J. Ward, F. Joseck, D. Gohlke, A. Lindauer, T. Ramsden, M. Bidy, M. Alexander, S. Barnhart, I. Sutherland, L. Verduzco and T. Wallington, *Cradle-to-Grave Lifecycle Analysis of U.S. Light Duty Vehicle-Fuel Pathways: A Greenhouse Gas Emissions and Economic Assessment of Current (2015) and Future (2025-2030) Technologies*, United States, 2016.
67. M. Aresta, A. Dibenedetto and A. Angelini, *Journal of CO2 Utilization*, 2013, **3-4**, 65-73.
68. E. Alper and O. Yuksel Orhan, *Petroleum*, 2017, **3**, 109-126.
69. F. D. Meylan, V. Moreau and S. Erkman, *Journal of CO2 Utilization*, 2015, **12**, 101-108.
70. M. R. Hamilton, H. J. Herzog and J. E. Parsons, *Energy Procedia*, 2009, **1**, 4487-4494.
71. K. Roh, H. Lim, W. Chung, J. Oh, H. Yoo, A. S. Al-Hunaidy, H. Imran and J. H. Lee, *Journal of CO2 Utilization*, 2018, **26**, 60-69.
72. X. Su, X. Yang, B. Zhao and Y. Huang, *Journal of Energy Chemistry*, 2017, **26**, 854-867.
73. J. Rostrup-Nielsen, *Journal of Molecular Catalysis A: Chemical*, 2000, **163**, 157-162.
74. S. Mitchell, N.-L. Michels and J. Pérez-Ramírez, *Chemical Society Reviews*, 2013, **42**, 6094-6112.
75. M. Campanati, G. Fornasari and A. Vaccari, *Catalysis Today*, 2003, **77**, 299-314.
76. P. Vibhatavata, J.-M. Borgard, M. Tabarant, D. Bianchi and C. Mansilla, *International Journal of Hydrogen Energy*, 2013, **38**, 6397-6405.
77. F. DiMascio, D. R. Hardy, M. K. Lewis, H. D. Willauer and F. Williams, *U.S. Patent No. 9,303,323*, 2016, Washington, DC: U.S. Patent and Trademark Office.
78. F. DiMascio, H. D. Willauer, D. R. Hardy, F. Williams and M. K. Lewis, *U.S. Patent No. 9,719,178*, 2017, Washington, DC: U.S. Patent and Trademark Office.
79. F. DiMascio, H. D. Willauer, D. R. Hardy, F. Williams and M. K. Lewis, *U.S. Patent No. 10,450,661*, 2019, Washington, DC: U.S. Patent and Trademark Office.
80. R. W. Dorner, D. R. Hardy, F. W. Williams and H. D. Willauer, *Energy & Environmental Science*, 2010, **3**, 884.
81. U. S. DOE, U.S. Department of Energy Announces \$110M for Carbon Capture, Utilization, and Storage, <https://www.energy.gov/articles/us-department-energy-announces-110m-carbon-capture-utilization-and-storage>, (accessed 4/19/2020, 2020).
82. C. E. Billings and W. R. Matson, *Science*, 1972, **176**, 1232-1233.
83. O. I. Joensuu, *Science*, 1971, **172**, 1027-1028.
84. D. S. Mallapragada, N. R. Singh, V. Curteanu and R. Agrawal, *Industrial & Engineering Chemistry Research*, 2013, **52**, 5136-5144.
85. R. G. Grim, Z. Huang, M. T. Guarnieri, J. R. Ferrell, L. Tao and J. A. Schaidle, *Energy & Environmental Science*, 2020, **13**, 472-494.
86. G. Liu, D. Willcox, M. Garland and H. H. Kung, *Journal of Catalysis*, 1984, **90**, 139-146.
87. D. Milani, R. Khalilpour, G. Zahedi and A. Abbas, *Journal of CO2 Utilization*, 2015, **10**, 12-22.
88. S. S. Iyer, T. Renganathan, S. Pushpavanam, M. Vasudeva Kumar and N. Kaisare, *Journal of CO2 Utilization*, 2015, **10**, 95-104.
89. Q. Smejkal, U. Rodemerck, E. Wagner and M. Baerns, *Chemie Ingenieur Technik*, 2014, **86**, 679-686.
90. G. Centi and S. Perathoner, in *Green Carbon Dioxide*, eds. G. Centi and S. Perathoner, 2014, DOI: 10.1002/9781118831922.ch1, pp. 1-24.
91. S. Mathesius, M. Hofmann, K. Caldeira and H. J. Schellnhuber, *Nature Climate Change*, 2015, **5**, 1107-1113.
92. P. Chen, G. Zhao, X.-R. Shi, J. Zhu, J. Ding and Y. Lu, *iScience*, 2019, **17**, 315-324.
93. M. R. Gogate and R. J. Davis, *Catalysis Communications*, 2010, **11**, 901-906.